QUANTUM TRANSPORT STRAIN ENGINEERING IN GRAPHENE

Guoqing Wei

A thesis
in
The Department
of
Physics

Presented in Partial Fulfillment of the Requirements
For the Degree of Master of Science
Concordia University
Montréal, Québec, Canada

January 2021

Concordia University
School of Graduate Studies

This is to certify that the thesis prepared

By: **Guoqing Wei**

Entitled: **Quantum Transport Strain Engineering in Graphene**

and submitted in partial fulfillment of the requirements for the degree of

Master of Science

complies with the regulations of this University and meets the accepted standards with respect to originality and quality.

Signed by the final examining commitee:

_____ Examiner

Dr. Valter Zazubovits

_____ Examiner

Dr. Ingo Salzmann

_____ Supervisor

Dr. Alexandre Champagne

Approved _____

Valter Zazubovits, Graduate Program Director

_____ 20 _____ _____

Pascale Sicotte, Dean of the Faculty of Arts and Science

Abstract

Quantum Transport Strain Engineering in Graphene

Guoqing Wei

We measure ballistic charge conductivity in strained suspended graphene and observe theoretically predicted [1] strain-induced scalar and vector potentials. To do so, we built an experimental platform for quantum transport strain engineering in 2D materials. This instrumentation permits low temperature (0.3 K- 70 K) transport and a tunable uniaxial strain (up to 3 %) which is independent from the gate-tunable charge density. We show slippage-free clamping of high aspect-ratio graphene crystals where atomically ordered edges are unnecessary for quantitative straintronics. We perform in-depth study of transport in a graphene channel with length 90 nm and width 600 nm. We observe ballistic transport in both the naked graphene channel and metal-film-coated graphene contacts. Through the strain-induced scalar potential, we can down shift the low energy band structure of the graphene channel by 20 meV. We also clearly observe the effect of a gauge vector potential, which reversibly suppresses the conductance by up to 13.6 %.

Acknowledgments

It was not easy. Despite that I am used to overcome challenges by my own; I could not complete my MSc without substantial help along the way. I cannot possibly express the amount of gratitude I feel toward all those who have positive influences on me. I will try my best to include all of their names here.

Firstly, I want to thank my supervisor Dr. Alexandre Champagne for his patience, helpful discussion, intuition, enthusiasm, and support during my MSc career. I have always been impressed by Alex's understanding of everyone's project in the group. As he is able to give people directions and correct them at anytime.

Next, I want to acknowledge the Champagne Group, thank you for your help in the lab. I thank Israel and Linxiang for the company of fabrication times especially at polytechnique. I thank Gareth for teaching me software we used in research. I acknowledge Matthew, Marc and Andrew for the training and advice of the instruments, and teaching me physics. I Thank Matthew for the tea break we used to enjoy in the office. I Thank Marc for being an excellent comedian as well as being an excellent researcher, I always have fun when spending time with you. I Thank Andrew for pass this interesting project to me, and answer all my questions patiently. My thanks to all the members of the Champagne Group for their friendship.

I would also like to thank Wentworth, first for his understanding of the IT conditions in our lab, second for his help for TA when I am writing my thesis.

To my parents, thank you for you support, understanding and no giving me pressure even though my degree takes much longer to finish then expected.

Contribution of Authors

I want to clarify that:

Andrew McRae took the leadership in developing the applied theory present in Chapter 2. We published this work together where he is the first author and I am the second author. Andrew McRae built the instrumentation for GQST transport measurements mentioned in Chapter 3. Andrew McRae also fabricated and measurement the device that I analysed in Chapter 4. The works done presented in this thesis will lead to a new publication where Andrew McRae and I will both be co-first author.

Contents

List of Figures

List of Tables

Chapter 1

Introduction to the straintronics of Graphene

Studies on quantum nano electro mechanical systems (QNEMS) lead to many promising properties and applications of 2D and 1D materials [2–5]. However, these contributions are often impeded by mechanical/electro-mechanical disorder. Using mechanical strain to optimize and manipulate the electronics of QNEMS is a sub-field of straintronics. In the field of straintronics [6], 2D materials and devices are controlled with mechanical constraints. This field overlaps with valleytronics, quantum computing, strain transistors, topological insulator strain sensors and superconducting straintronic devices [1, 7–12]. So far, our main contribution to this field has been the proposal of a platform with *in situ* tunable strains at low temperatures to study the strain-engineering of quantum transport in graphene [1]. Where my main contributions to the project are: help to complete our applied theory such as parameters verification, test the code of the model so it is vaild under all condition, code maintenance and debug, extending our graphene applied model to SWCNT; Developing Fabrication methods on silicon wafers with ultra-thin SiO_2 layers for next generation suspended graphene devices and performing data analysis for the experiment that we reporting. In this thesis, we also report the detailed data analysis of an experiment with such a platform and compare its results with our theoretical predictions.

We begin this chapter with a brief introduction to graphene QNEMS and how uniaxial strain affects them. We review recent progress in related 2D materials straintronics in the literature to provide a context for our work. We highlight the

advantages of our platform for strain-engineering transport studies compared to other approaches. We conclude with an outline of this thesis, which studies strain-tunable suspended graphene field effect transistors (FETs) as shown in Fig. 1.1.

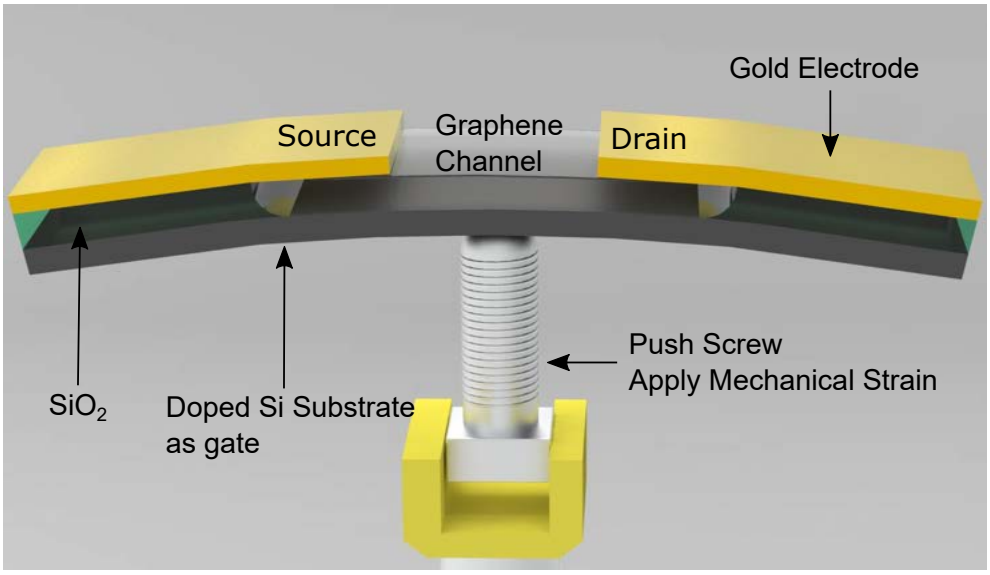

Figure 1.1: 3D schematic diagram of our quantum straintronics platform device. A suspended graphene is clamped by gold cantilevers. A push screw bends the silicon substrate and elongate the suspended graphene where a uniform uniaxial strain is generated.

1.1 Graphene: Ideal QNEMS for Strain-Enginnering

Graphene is an ideal QNEMS due to its large elastic deformation range [13], long mean free-path [14], and strong electromechanical coupling [15]. Monolayer graphene is a single layer of carbon atoms assembled into a honeycomb lattice, as shown in Fig. 1.2(a). Another material that has similar properties to monolayer graphene are single-wall carbon nanotubes (SWCNTs), which are a rolled up monolayer graphene sheets. The SWCNT structure is shown in Fig. 1.2(b). Single atom thickness crystal like graphene and SWCNT are very sensitive to mechanical deformations. Graphene lattice has a large elastic range of deformation because its sp^2 bonds require lots of energy to break. Theoretically, graphene can support up to 30% of strain [13] without fracture. Similarly, carbon nanotubes are also mechanically robust and flexible, and can hold up to 16% of strain [16].

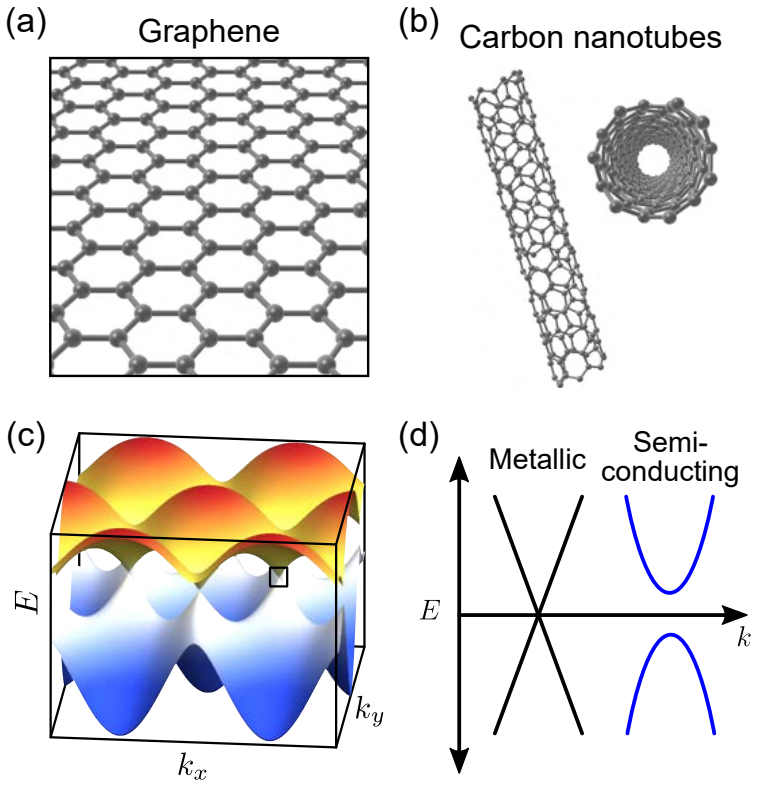

Figure 1.2: Lattice and band structure of monolayer graphene and SWCNTs. (a) Graphene real-space crystal lattice. (b) SWCNT real-space structure. (c) Graphene band structure. The low-energy dispersion (Dirac cone) is highlighted by the black box. (d) The low-energy carbon nanotube band structure can be metallic or semiconducting. This figure was reproduced from [17].

Graphene has exceptional electronic properties in addition to its mechanical properties. We show graphene's band structure in Fig. 1.2(c). The valence bands (blue) and conduction bands (red) touch at points, called Dirac points, see Fig. 1.2(c), making graphene semimetallic. Graphene has electron mobilities measured up to $3,000,000$ V^{-1} s^{-1} at 1.8 K, and with mean free paths up to $\ell \sim 1$ μm at room temperature [18]. Which open to prospect of room temperature quantum (phase-preserving) circuits. The low-energy dispersion of electrons is linear, leading to relativistic like transport. This leads to novel "electron optics" devices, where the charge carriers (electrons or holes) can be manipulated analogously to light, reflecting or refracting at potential boundaries [19]. The strong and tunable coupling between its robust mechanics and unique electronics makes graphene ideal for QNEMS research.

We show the carbon nanotube band structure in Fig.1.2(d). While graphene is semimetallic, carbon nanotubes can be either semimetallic or semiconducting depending on how they are rolled [20]. Semiconducting tubes make excellent transistors, and recently a computer was made entirely from carbon nanotube transistors [21].

The electronic band structure of graphene is highly sensitive to strain, which leads to strong electromechanical coupling [15]. Specifically, a strain induces scalar potential $\Delta\mu_\varepsilon$, and vector potential $\boldsymbol{A}$, modify quantum transport in graphene. In Fig. 1.3(a)–(b), we show the effect of $\Delta\mu_\varepsilon$ on the low energy dispersion (Dirac cones) of graphene. As we apply strain, the scalar potential changes the work function of graphene, and shift its Fermi level. In Fig. 1.3(c)–(d), we show respectively full view and zoomed-in views of graphene's first Brillouin zone, Where the effects of $\boldsymbol{A}$ is visible. Indicated by the blue arrows, the vector potentials act to displace Dirac points in momentum space. For instance, moving the black Fermi circle $\boldsymbol{K}^{'}$ to the red circle $\boldsymbol{K}^{'}_{D}$ as strain is applied. The dashed lines show the unstrained (black) and strained (red) first Brillouin zones. At the K and K' points, the vector potential points in opposite directions [15]. When strain deforms the lattice, the changes in atomic spacing and electron hopping energy are represented by these gauge potentials $\boldsymbol{A}$. Uniaxial-strain leads to uniform $\boldsymbol{A}$, which can suppress the transmission probability at strain interfaces (like at the interface of two dielectrics in optics) [10, 22]. Tri-axial strains can on the other hand, generate a uniform pseudomagnetic field up to $B_{\mathrm{ps}} = \nabla \times \boldsymbol{A} \sim 800$ T [23, 24], with opposite values in the K, K' valleys. Controlling such phenomena would permit the study of pseudomagnetic quantum Hall effects and Landau levels at room temperature,

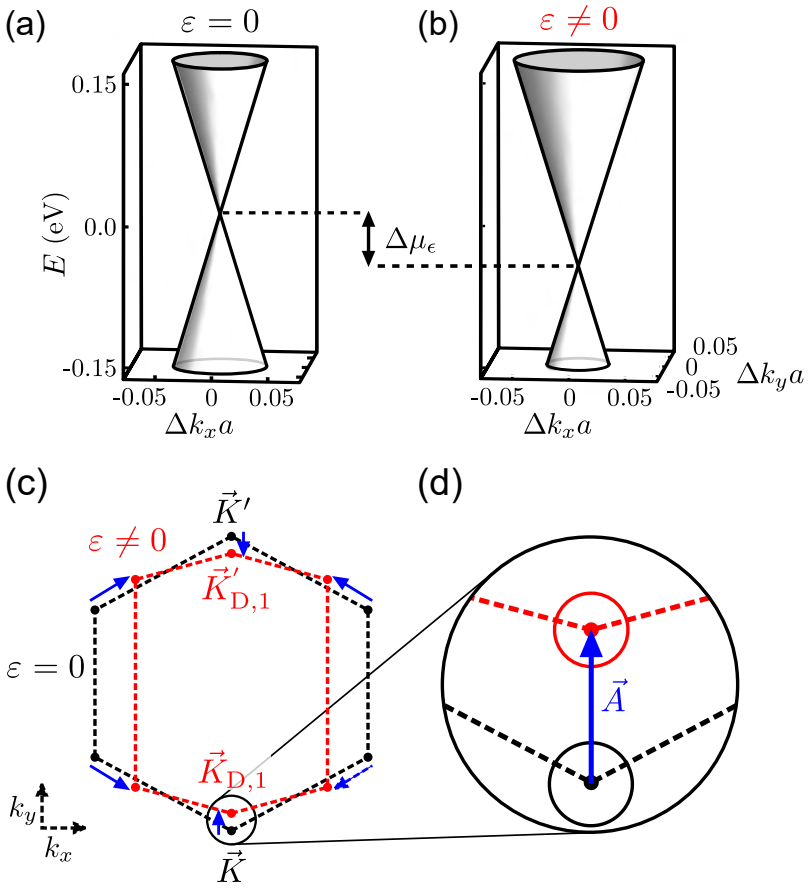

Figure 1.3: Strain-induced scalar and vector potentials. (a)–(b) Unstrained and strained Dirac cone of graphene. Strain induces a scalar potential ($\Delta\mu_\varepsilon$), which shifts the Dirac cone. (c) The first Brillouin zone of graphene showing the Dirac points in unstrained ($\boldsymbol{K}'$, black circles) and strained ($\boldsymbol{K}'_D$, red circles). The dashed lines outline the first Brillouin zones of the unstrained (black) and strained (red) lattice, and blue arrows indicate the direction and magnitude of the vector potentials $\boldsymbol{A}$. (d) Shows a close-up view of the vector potential, representing the strain-induced shift of the Dirac point. This figure was reproduced from [17].

and other effects such as valleytronics [24, 25].

1.2 Recent Experiments on Strained Carbon Nanoelectronic Devices

While there are many theoretical proposals in graphene straintronics, progress in experimental strain-engineering of quantum transport has been very slow in literature. This is due to the complexity of instrumentation and devices needed to strain QNEMS at low temperature. In order to study straintronics in graphene and carbon nanotubes QNEMS, we require a system able to apply tunable, stable in time, and spatially uniform strains inside a low temperature electron transport cryostat. To our knowledge, we are the only group to propose to meet all of the requirement with our nanofabricated devices and custom built instruments [1]. Still, there are many other approaches being pursued to study strained transport in graphene and carbon nanotubes. Here, we review a few examples of experimental results in the literature, to provide the context in which the contributions of the thesis are made.

Strain field can be induced by nanopatterning of the substrate topography [26,30,31]. Creating nanobubbles or wrinkles in a graphene sheet [32] were studied to observe strain effects on thermal conductivity and the creation of pseudomagnetic fields in graphene. An example of a substrate-induced strain fields (static fields), is shown in Fig. 1.4(a) [26]. Boron nitride nanopillars were used to locally stretch a graphene crystal, resulting in pseudo Landau levels, which could be observed by scanning tunnelling spectroscopy (local measurement). This method is good to study the consequent of strain on local band structure but not transport, moreover tunable strains are not allowed by this set-up. In Fig. 1.4(b) [27], we show an experiment where a local strain is induced in graphene by Gaussian bump induced by the tip of a scanning tunnelling microscope. This can achieve large pseudomagnetic fields ~ 1000 T. The plot shows the measurement of the local density of states modified by the pseudomagnetic fields. Even though this method applies a tunable local strain and result in large pseudomagnetic fields, it is not suitable for strained transport experiment which require long-range control over strain. Such local strains would be very hard to model for transport because disorder on short scale would dominate transport. Other approaches include strain applied by pushing on graphene with

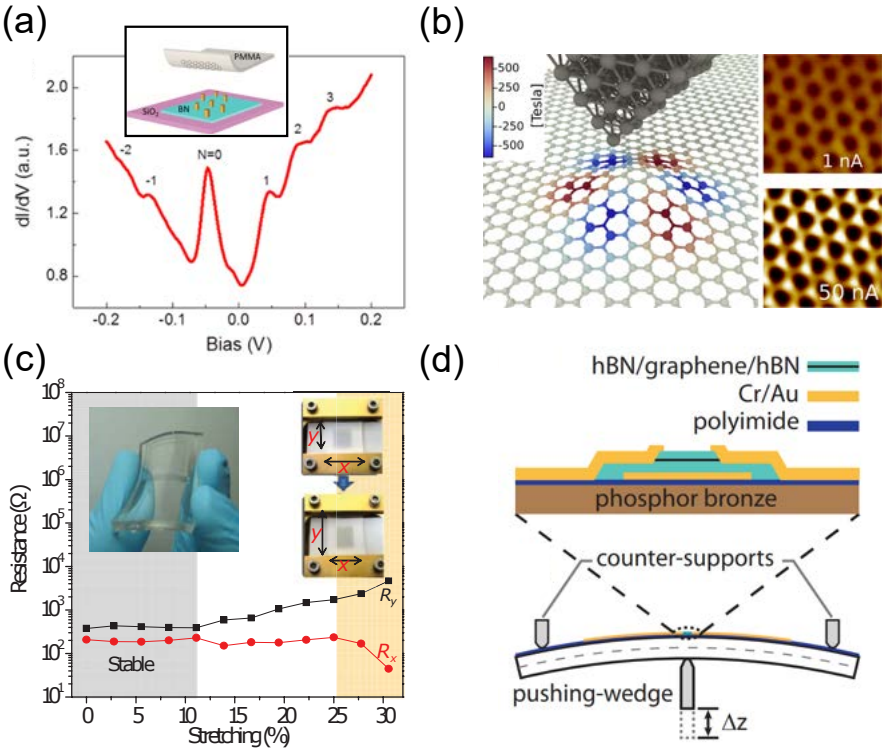

Figure 1.4: Literature review of Experimental methods for straining graphene. (a) Inset: patterned substrate to strain graphene. Depositing a graphene sheet on boron nitride pillars imparts a strain field. Main panel: differential conductance STM data as a function of bias voltage, showing pseudo-Landau levels (index N) [26]. (b) Locally strained graphene using a STM electrostatic pull. Extreme pseudomagnetic fields ($B_{\mathrm{ps}} \sim 1000$ T) were achieved STM images taken at tip current 1 nA and 50 nA (right), show the B_{ps}-modified local density of states. [27]. (c) Tunable strain using flexible substrates. Top left inset: bendable graphene device on PDMS (Polydimethylsiloxane). Top right insets: controllably straining graphene along two axes. Main panel: Classical resistance change with up to 30% strain in graphene [28]. (d) Encapsulated graphene channel strained with a pushing-wedge [29].

atomic force microscope (AFM) tips [33], but this method is not easily compatible with low temperature transport measurements, the strain applied by the AFM tip is poorly controlled. Strains have also been induced by clamping graphene on stretchable substrates [28, 34], or using microelectromechanical systems (MEMS) comb drive actuators [35] while performing Raman spectroscopy and conductivity measurements. An example of such a stretchable substrate graphene device is shown in Fig. 1.4(c) [28]. The insets show that the substrate is bendable. The main plot displays resistance versus strain up to 30% along the x and y axes. Despite their large strain-tunability, stretchable substrates are mostly limited to room temperature, and often cause local mechanical disorder in the graphene sheet. Tunable strains have been applied to suspended graphene sheets using electrostatic forces form a back gate [36, 37]. These strains were small $\sim$ 0.01–0.1%, and are not independent from the charge carrier density changes in the graphene sheet. Fig. 1.4(d) shows a more advanced platform with *in situ* tunable strain. However, once again this method is limited to small strains, and difficult to use at low temperature.

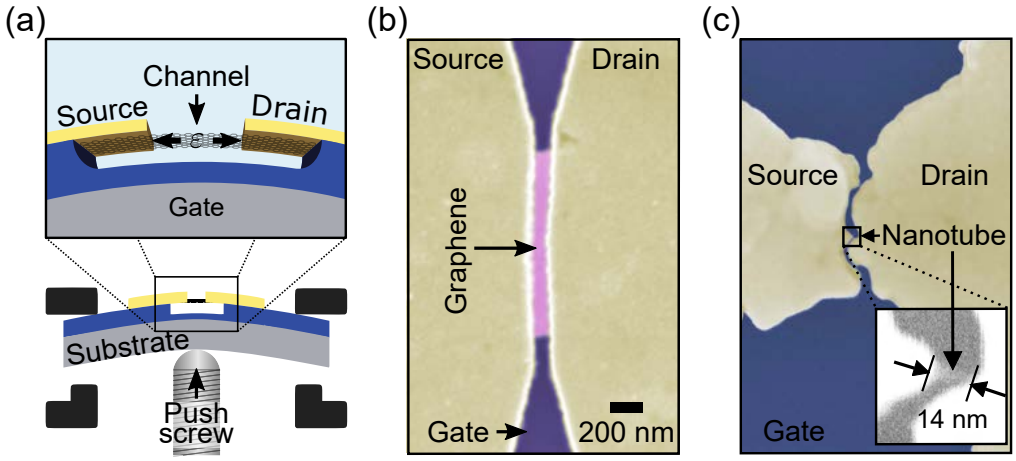

Figure 1.5: Our strain instrumentation and devices for ultra-short carbon devices. (a) Schematic diagram of our QTSE instrumentation. (bottom) A push screw bends the sample substrate, imparting a strain on the suspended channel. (top) A more detailed view of the strained device, showing the strained suspended channel, and source/drain/gate electrodes used for electron transport measurements. (b)–(c) False coloured scanning electron micrograph of suspended 100-nm long graphene and 14-nm long carbon nanotube channels respectively. The inset in panel (c) shows the nanotube channel in greater detail. Reproduced from [17].

Our set-up, shown in Fig. 1.5 and Fig. 1.1 has a geometry similar to The

metal–oxide–semiconductor field-effect transistors (MOSFETs). Where the metal is replaced by a doped silicon substrate. Our platform applies strains by bending the substrate with a push screw drive by a digital-control motor. Where we can apply continuous and tunable strain. The channel is suspended between the two long gold cantilevers which stretch the channel when the substrate is bent. The strain is completely decoupled from the charge density in the channel. This platform is compatible with low temperature measurements thanks to our custom instrumentation [17] integrated into a 0.3 K cryostat. Our platform allows graphene, carbon nanotubes, or other 2D and 1D materials to be studied, as shown in Fig. 1.5(b)–(c).

1.3 Outline of this Thesis

In this thesis, we report a complete experiment on quantum transport in strained graphene. Combine with our applied theory [1], we show deep understanding to our data that displays changes of graphene work function, suppression of conductance and quantum interference, which are evidences for strain-induced scalar and vector potentials.

In Chapter 2, we summarize our applied theory [1]. We start by presenting the Dirac Hamiltonian for strain graphene transistors. We show the mathematical expression of the strain-induced gauge potentials $\boldsymbol{A}$. We derive the transmission followed by our theoretical predictions. And the extension toward SWCNT at the end.

In Chapter 3, we report our fabrication methods for low-disorder suspended graphene FETs designed for strain-engineering experiments. Where the 3 main steps are: Exfoliate highly-crystalline monolayer graphene samples onto silicon wafers with prepared oxide thickness and coordinate grids. defined source and drain electrodes by lithography. liberate the graphene sample by wet-etching.

In Chapter 4, we present our first experiment performed on our proposed platform. We first show the geometry of the device. Then we demonstrate how to calculate and extract parameters from the processed data. We compare experimental data with our theoretical predictions after, where we find agreements.

In Chapter 5, we summarize the key results presented in this thesis, and discuss the outlook for future experiments in strain-engineering transport experiment on 2D and 1D materials.

Chapter 2

Applied Theoretical Model for Graphene Quantum Strain Transistors(GQSTs)

Inspired by the possibility that uniaxial strain can completely suppress conductivity in graphene [10, 22, 38], We propose a new type of device called graphene quantum strain transistors(GQSTs) [1]. These GQSTs' conductivity could turn off because uniaxial strain can tailor the energy, momentum, and quantum transmission of charge carriers in graphene [14], even without any bandgap. However, even after a decade of the first proposal [10], there is no a clear experimental approach to achieve GQSTs. Two of the main challenges are: the lack of a suitable experimental platform allowing *in situ* low-temperature tuning of strain in 2D Materials. The hypersensitivity of 2D Materials to their environment. Thus, it is difficult to describe or predict experiment results with idealized models. Therefore, we propose our own experimental platform, as shown in Fig. 2.1 and applied theoretical model to achieve uniaxial strain engineering of quantum transport in graphene or other 2D materials. The theoretical concepts of the platform will be present in this chapter, while the construction and operation of the instrumentation will be presented in the following Chapter. Based on this realistic platform design, we have developed an applied theory to guide and analyse experiments. This model includes all relevant experimental parameters and limitations from our platform and devices.

Section. 2.1 summarizes the applied model, which is published as [1], where I am

the 2nd author of the paper. Section. 2.1.2 presents the extension of the applied model to SWCNT strain transistors, where I integrate the SWCNT boundary condition to the applied model. The full applied model for SWCNT is continued by Linxiang Huang.

2.1 Summary of the Applied GQST Model

In this section, we will present our applied theory aimed at guiding our experiments towards Graphene Quantum Strain Transistors (GQSTs). First, we present proposed experimental platform. This platform will permit the study of uniaxial strain in 2D materials. Secondly, we describe the theoretical model based on the platform. We consider all sources of strain and strain effects on graphene's band structure. We find that a strain-induced scalar potential and vector potential play dominant role. Identify their unique transport signatures, namely the strain-induced scalar potential shifts the Dirac point of the graphene and the strain-induced vector potential suppress charge conductivity. Combining these effects, we find that GQSTs are feasible. We determine graphene orientations which allows total suppression of conductivity. Thirdly, we will present our most recent extension to single-wall carbon nanotubes (SWCNTs).

2.1.1 Proposed Experimental Platform

The proposed platform is shown in Fig. 2.1. It could be used to study strain engineering in 2D or 1D materials. Here we focus on suspended graphene devices where channel dimensions are $L = 100$ nm and $W = 1000$ nm, which are a reasonable dimension for nanofabrication. The gold films covering the graphene contacts, inject current into and dope the source and drain contacts [39, 40]. We make the $W/L \gg 1$ to greatly suppress the effect of edge disorder in the suspended graphene crystal. It then becomes realistic to use an analytic ballistic transport model with a smooth boundary condition [41].

The zoomed in part of Fig. 2.1(a) shows the graphene lattice and crystal orientation, θ, defined as the angle between the x-axis of the device and the zig-zag direction of the crystal. This angle could be measured prior to gold film deposition using polarized Raman spectroscopy [42], or via STM imaging [43].

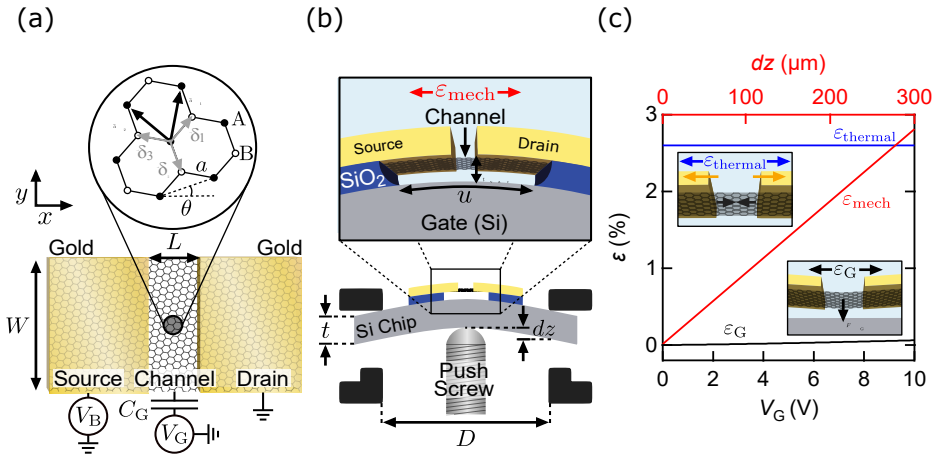

Figure 2.1: Platform for uniaxial quantum transport strain-engineering (QTSE) in graphene. (a) Top-down view of the proposed ballistic graphene transistor geometry. Inset: the graphene lattice, showing the crystal orientation θ with respect to the x-axis of the device. (b) Side view of the proposed graphene device and mechanical strain instrumentation. The mechanical assembly bends the substrate, which strains the suspended channel. The inset shows a close-up view of the suspended device geometry. (c) The three sources of strain in the channel: the thermal contraction (blue) at $\sim$ 1 Kelvin, the mechanical motion (red, top axis) of the push screw, and electrostatic strain (black, bottom axis) from the gate voltage, V_G. Insets: visualizing the strain imparted by the gold and graphene thermal expansion (top left), and electrostatic pulling (bottom right).

Figure 2.1(b) shows the suspension of the channel, and how to apply mechanically-tunable strains using a push screw. The suspended gold cantilevers have a thickness of 100 nm. When the silicon substrate is bent, the gold cantilevers stretch the channel. The expected mechanical strain $\varepsilon_{\text{mech}}$ applied by this instrumentation can be estimated by [44]:

$$\varepsilon_{\text{mech}} = \frac{3ut}{2D^2}\frac{dz}{L} \tag{2.1}$$

Where L is the suspended channel length, $t = 200$ μm is the thickness of the substrate, $D = 8.2$mm is the clamping distance, $u = 1$ μm is the total cantilevers and channel suspension length, while dz is the vertical displacement of the push screw. Based on previous experiments [44], the range of dz is up to 300 μm, giving a maximum mechanical strain $\approx \varepsilon_{\text{mech}}^{\text{max}} \approx 2.8\%$. In our calculations, we will set maximum mechanical strain $\varepsilon_{\text{mech}}^{\text{max}} = 2.5\%$.

We calculate the gate capacitance per unit area by treating the space between the gate and the channel as two capacitors in series:

$$c_G = \frac{\epsilon_{\text{vac}}\epsilon_{ox}}{t_{ox}\epsilon_{\text{vac}} + t_{\text{vac}}\epsilon_{\text{vac}}} \tag{2.2}$$

Where $t_{\text{vac}} = 50$ nm is the suspension height of the channel, $t_{ox} = 150$ nm is the remaining thickness of the oxide. ϵ_{vac} is the vacuum permittivity, and ϵ_{ox} is the permittivity of SiO_2. We find a gate capacitance per unit area of $\approx 3.7 \times 10^{-9}$ F/cm^2.

Figure 2.1(c) shows the sources of strain we have consider in our model. The mechanically-tunable strain, $\varepsilon_{\text{mech}}$ is provided by the instrumentation and determined by Equation 2.1, with a range of $\varepsilon_{\text{mech}} \leq 2.5\%$. The thermally induced strain $\varepsilon_{\text{thermal}}$ comes from cooling of devices to ultra low temperature, less than 1 Kevin, which contracts the gold cantilevers [45], while the graphene slightly expands [46]. This $\varepsilon_{\text{thermal}}$ is by:

$$\varepsilon_{\text{thermal}} = -\frac{u-L}{L}\int_{300}^{T}\alpha_{\text{Au}}(t)dt - \int_{300}^{T}\alpha_{\text{g}}(t)dt, \tag{2.3}$$

where α_{Au} and α_{g} are the coefficients of thermal expansion for gold and graphene respectively. Using α_{Au} from Ref. [45] and α_{g} from Ref. [47], we calculate a net thermal strain of $\varepsilon_{\text{thermal}} = 2.5 \pm 0.1\%$ for $T \approx 1$ K.

The last source of strain in Fig 2.1(c) is electrostatic, ε_{G}, and caused by the electrostatic force stemming from a gate voltage. However, given the short length

of the channel, and the sturdiness of the gold cantilevers, we calculate that ε_{G} is negligibly small ($\approx 0.01\%$). Therefore, $\varepsilon_{\mathrm{total}} = \varepsilon_{\mathrm{thermal}} + \varepsilon_{\mathrm{G}} + \varepsilon_{\mathrm{mech}} = 2.6 - 5.1\%$. and is independent from the gate voltage which will be used to control charge density in the channel.

2.1.2 Theory of Uniaxial Strain-Engineering of Transport in Ballistic Graphene

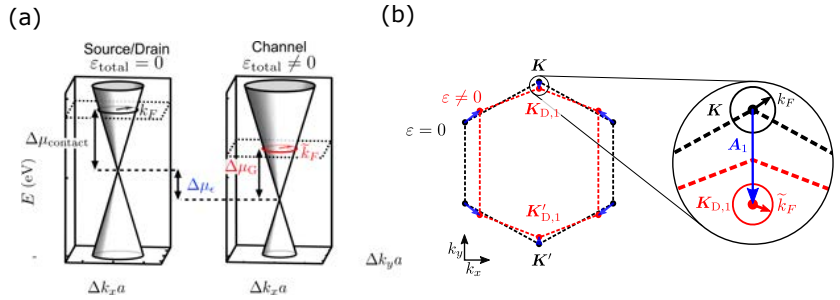

Figure 2.2: Applied theory for uniaxial strain tuning of graphene's band structure. (a) Dirac cone and Fermi circle in the unstrained (left) source/drain graphene contacts, and in the strained (right) graphene channel. (c) Unstrained (black) and uniaxially strained (red) first Brillouin zone (FBZ) of graphene. The strain value in this figure is exaggerated to $\varepsilon_{\mathrm{total}} = 20\%$ to make its effects more clearly visible. Under strain, the Dirac points shift can be used to define gauge vector potentials (blue arrows), $\boldsymbol{A}_i = \boldsymbol{A}_{\mathrm{lat},i} + \boldsymbol{A}_{\mathrm{hop}}$. The inset shows that the corner of the FBZ does not coincide with the Dirac point when the device is under strain.

In the ballistic transport regime, we can write the uniaxially strained graphene Hamiltonian as [1, 15]:

$$H_{K_i} = \hbar v_F(\bar{\boldsymbol{I}} + (1-\beta)\bar{\boldsymbol{\varepsilon}}) \cdot \boldsymbol{\sigma} \cdot (\tilde{k} \pm \boldsymbol{A}_i) + \Delta\mu_G + \Delta\mu_\varepsilon \tag{2.4}$$

Where v_F is the Fermi velocity in graphene, $\bar{\boldsymbol{I}}$ is the identity matrix, $\beta = -\partial \ln \gamma_0 / \partial \ln \gamma' \approx 2.5$ is the electronic Grüneisen parameter [15] Where $\gamma_0 = -2.7$ eV is the unstrained hopping energy [14], and the next nearest-neighbour hopping $\gamma' \approx -0.3$ eV [48]. $\bar{\boldsymbol{\varepsilon}}$ is the 2×2 strain tensor with elements $\varepsilon_{xx} = \varepsilon_{\mathrm{total}}$, $\varepsilon_{yy} = -\nu\varepsilon_{\mathrm{total}}$ and $\varepsilon_{xy} = \varepsilon_{yx} = 0$, where $\nu = 0.165$ is the Poisson ratio [15], and $\boldsymbol{\sigma} = (\sigma_x, \sigma_y)$ is the Pauli matrix vector in 2D and acts as a pseudospin operator. The gauge vector potentials $\boldsymbol{A}_i$ are used to describe the movement of the Dirac points in first Brillouin zone (FBZ) of strained graphene as shown in Fig 2.2(b), The electron's generalized wavevector is

then $\boldsymbol{k} - \boldsymbol{A}_i$, where the index $i = 1, 2, 3$ labels the three K_i. The plus-minus sign in Eq. 2.4 corresponds to the K and K' valleys respectively.

Figure 2.2(a) shows the low energy band dispersion and Fermi circle around a Dirac point in the source/drain graphene contacts (left) and the strained channel (right). The Fermi level in the source/drain contacts $\Delta\mu_{\text{contact}}$ is determined by the contact doping due to charge transfer from Au. The Fermi wavevector in the source/drain contacts are $k_F = \Delta\mu_{\text{contact}}/\hbar v_F$. We set $\Delta\mu_{\text{contact}} = -0.12$ eV, which is typical of graphene under Au, and a number we obtained from a previous experiments [40]. Our conclusions are not sensitive to this number. In the channel, the band structure is shifted vertically in energy by uniaxial strain. This is modeled by a scalar potential $\Delta\mu_\varepsilon = g_\varepsilon(1-\nu)\varepsilon_{\text{total}}$ [49], where the coupling parameter $g_\varepsilon \approx 3.0$ eV, [50] The channel's Fermi wavevector $\tilde{k}_F$ depends on both the strain-induced energy shift $\Delta\mu_\varepsilon$ and the gate-induced one $\Delta\mu_G$, $\tilde{k}_F = (\Delta\mu_{\text{G}} + \Delta\mu_\varepsilon)/\hbar v_F$, where $\Delta\mu_{\text{G}} = \hbar v_F\sqrt{\pi c_{\text{G}} V_{\text{G}}/e}$, $v_F = 1.05 \times 10^6$ m/s [51].

The total gauge potentials are shown in Fig 2.2(b), $\boldsymbol{A}_i = \boldsymbol{A}_{\text{lat},i} + \boldsymbol{A}_{\text{hop}}$, where [1]:

$$\boldsymbol{A}_{\text{hop}} = \frac{\beta\varepsilon(1+\nu)}{2a}\begin{pmatrix}\cos 3\theta \\ \sin 3\theta\end{pmatrix} \tag{2.5a}$$

$$\boldsymbol{A}_{\text{lat},1} = \frac{4\pi\varepsilon}{3\sqrt{3}a}\begin{pmatrix}-\cos\theta \\ \nu\sin\theta\end{pmatrix} \tag{2.5b}$$

$$\boldsymbol{A}_{\text{lat},2} = \frac{2\pi\varepsilon}{3a}\begin{pmatrix}\frac{1}{\sqrt{3}}\cos\theta + \sin\theta \\ -\frac{1}{\sqrt{3}}\nu\sin\theta + \nu\cos\theta\end{pmatrix} \tag{2.5c}$$

$$\boldsymbol{A}_{\text{lat},3} = \frac{2\pi\varepsilon}{3a}\begin{pmatrix}\frac{1}{\sqrt{3}}\cos\theta - \sin\theta \\ -\frac{1}{\sqrt{3}}\nu\sin\theta - \nu\cos\theta\end{pmatrix} \tag{2.5d}$$

Strain-induced vector potential $\boldsymbol{A}_i$ distorts graphene lattice changing the shape of FBZ, and it moves Dirac points to new locations, change nearest-neighbor hopping energy. we also notice the curl of $\boldsymbol{A}_{\text{lat},i}$ is always zero [52], this may result in an Aharonov-Bohm like effect.

The strain-induced scalar and vector potentials affect transport. shown in Fig 2.3. The momentum wavevectors in the source and channel $k_F = \pm|k\hat{x} + q_n\hat{y}|$, and $\tilde{k}_F = \pm|\tilde{k}\hat{x} + \tilde{q}_n\hat{y}|$ respectively. The transverse (y-direction) boundary condition

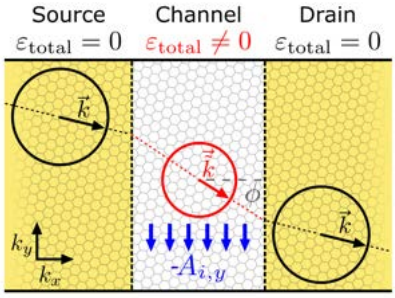

Figure 2.3: Transport in ballistic strained graphene. Charge carrier wavevectors in the source, channel, and drain of the uniaxially strained graphene transistor. The transmission modes are labelled with their y-component wave number q_n. The addition of $A_{i,y}$ in the channel modifies the propagation angle, and thus the transmission probability of the carriers.

conserves the y-momentum as carriers move between the contacts and the channel [10], thus we have $\tilde{q}_n = q_n - A_{i,y}$. Therefore, as shown in Fig!2.3, when a carrier enters the strained channel, its propagation angle will be modified by $\boldsymbol{A}_{i,y}$. The transmission probability depends on this angle and can be reduced to zero.

Using Eq. 2.4 and matching the carrier's wavefunction at the potential steps along x direction [41], and using a smooth y-direction boundary condition, we solve for the transmission probability $T_{\xi,i,n}$ of conduction mode n and valley $\xi = \pm 1, i = 1, 2, 3$. We find:

$$T_{\xi,i,n} = \frac{(v_x k\tilde{k})^2}{(v_x k\tilde{k})^2 \cos^2[\tilde{k}L] + (k_F \tilde{k}_F - v_y q_n (q_n - \xi \boldsymbol{A}_{i,y}))^2 \sin^2[\tilde{k}L]}, \tag{2.6}$$

where $q_n = \frac{\pi}{W}(n + \frac{1}{2})$ is the quantized transversal momentum for the mode n, $k = (k_F^2 - q_n^2)^{1/2}$, $\tilde{k} = v_x^{-1}[v_F^2 \tilde{k}_F^2 - v_y^2 (q_n - \xi A_{i,y})^2]^{1/2}$, $v_x = v_{F,xx}/v_F = (1 + (1 - \beta)\varepsilon_{\text{total}})$, and $v_y = v_{F,yy}/v_F = (1 - (1 - \beta)\nu\varepsilon_{\text{total}})$.

We can obtain the conductivity by summing all transmission modes:

$$\sigma = \frac{L}{W} \frac{2e^2}{h} \frac{1}{3} \sum_{\xi} \sum_{i}^{3} \sum_{n}^{N} T_{\xi,i,n}, \tag{2.7}$$

where $N = \text{Int}(k_F W/\pi + \frac{1}{2})$ is the number of allowed modes set by the contact's Fermi level, and the factor $\frac{1}{3}$ takes care of the three-fold K and K' point degeneracy

in unstrained graphene.

For the parameters discussed above: $\varepsilon_{\text{thermal}} = 2.6$ %, $\Delta\mu_{\text{contact}} = -0.12$ eV, $L = 100$ nm and $W = 1000$ nm. We explore theoretically the experimentally relevant regime where $k_B T \sim 0.1$ meV $< eV_{\text{B}} < 1$ meV $\ll \Delta\mu_{\text{contact}} = 0.12$ eV, and $\hbar v_F A_{i,y}$ reaches up to 0.34 eV at maximum=$\varepsilon_{\text{total}} = 5.1\%$ when $\theta_{crystal} = 30°$. We calculate the conductivity for different strains, crystal orientation and gate voltages. In Fig. 2.4, we show plots of $\sigma - \varepsilon_{\text{mech}} - V_{\text{G}}$ at three $\theta_{crystal} = 0°, 15°, 30°$. We predict two clear experimental transport signatures: a gate-shift of the conductivity minimum, which indicates a shift of Dirac points, due to $\Delta\mu_{\varepsilon}$, and a suppression in conductivity at all gate voltages, stemming from $\boldsymbol{A} - i$'s.

In Fig. 2.4(a), $\theta_{crystal} = 0°$, and at this crystal orientation the vectors $\boldsymbol{A}_{i,y}$ are small as given by equation 2.5. The scalar potential dominates. Dirac point's gate voltage position is described by:

$$V_{\text{D}} = -\frac{e}{C_{\text{G}}} \frac{g_{\varepsilon}^2}{\pi(\hbar v_F)^2} (1-\nu)^2 \varepsilon_{\text{total}}^2 \tag{2.8}$$

In Fig. 2.4(b), we can see how the vector potentials affect the transport. The conductivity decrease as strain increases. This effect is maximized When $\theta = 30°$ in Fig. 2.4(c), where we find a region where the conductivity is completely suppressed, starting at $\varepsilon_{\text{mech}}$=0.5%. Thus, a graphene quantum strain transistor is predicted under these realistic conditions.

In Fig. 2.5, we show $\sigma - V_{\text{G}}$ at $\varepsilon_{\text{mech}} = 2.5\%$ and $\theta_{crystal} = 30°$. We observe that a high on/off ratios ($\sigma_{\text{on/off}} > 10^4$) can be reach for a wide range of gate voltages. Figure. 2.5 is a colour map of the $\sigma_{\text{on/off}}$ ratio extracted from data similar to Fig. 2.5(a) within $V_{\text{G}} = \pm 10$ V. We map this on/off ratio as a function of the contact doping $\Delta\mu_{\text{contact}}$ and the lattice orientation $\theta_{crystal}$. We find that to reach $\sigma_{\text{on/off}} > 10^4$, when $\varepsilon_{\text{total}} = 5.1\%$ and $|\Delta\mu_{\text{contact}}| \leq 0.12$ eV, $\theta_{crystal} \geq 16°$ is required. This requirement defines a broad region of parameter space, shown in red and whose boundary is drawn with a solid black line. This broad range of possible parameters makes it likely to observe a high on/off ratio GQST effect in realistic experimental devices.

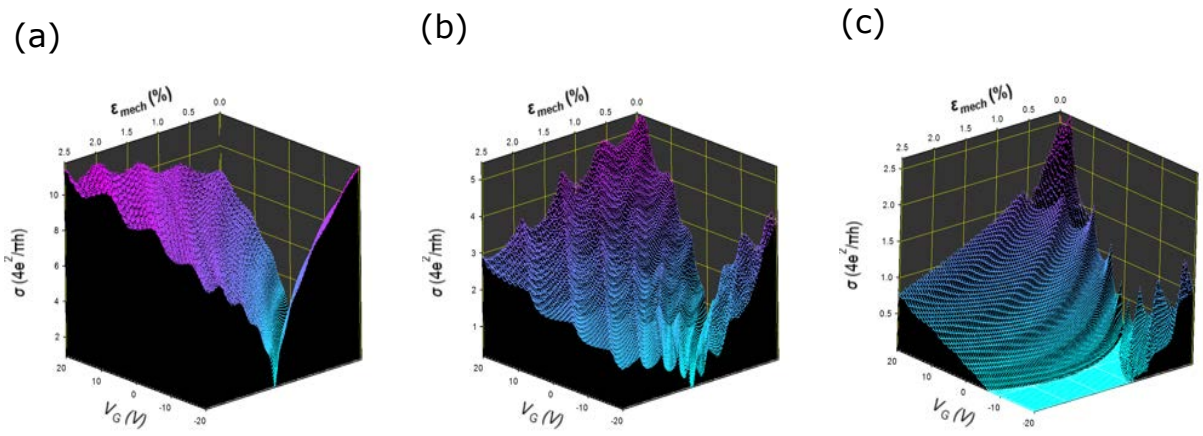

Figure 2.4: Conductivity signatures of uniaxial QTSE in graphene.(a) $\sigma - V_{\rm G} - \varepsilon_{\rm mech}$ data at $\theta = 0°$. The strain-induced $\Delta\mu_{textmech}$ shifts the minimum σ towards negative $V_{\rm G}$. The inset shows the gate-shift of the Dirac point, V_D, as a function of $\varepsilon_{\rm mech}$ up to 1.5%. (b) $\sigma - V_{\rm G} - \varepsilon_{\rm mech}$ = at $\theta = 15°$. There is a rapid decrease in σ with strain. Fabry-Pérot resonances are clearly visible, and their spacing $\Delta V_{\rm FP}$ is strain dependent. (c) $\sigma - V_{\rm G} - \varepsilon_{\rm mech}$ = data at $\theta = 30°$ show a complete suppression of σ at higher strains.

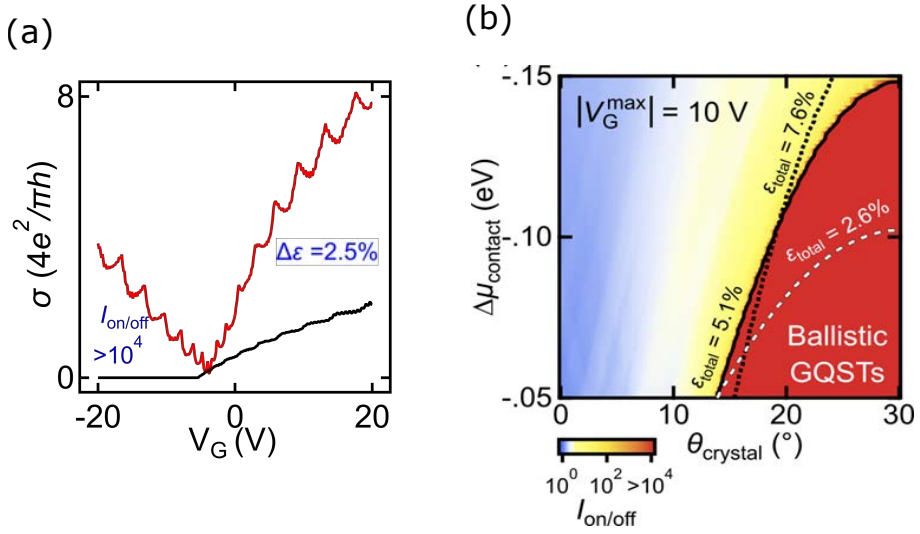

Figure 2.5: Graphene quantum strain transistors (GQSTs). (a) $\sigma - V_{\rm G}$ for $\varepsilon_{\rm total} = 0\%$ (black) $\varepsilon_{\rm total} = 5.1\%$ (red) and $\theta = 30°$. The 50 nm gate spacing gives rise to a dramatic GQST effect with $\sigma_{\rm on/off} \gg 10^4$. (b) $\sigma_{\rm on/off} - \Delta\mu_{\rm contact} - \theta$ colour maps for respectively $V_{\rm G}^{\rm max} = \pm$ 10 V. The solid and dashed lines show the $\sigma_{\rm on/off} > 10^4$ boundaries for total strain values of $\varepsilon_{\rm total} = 2.6\%$, and 5.1% respectively.

2.2 Extension of the Applied Model to SWCNT Strain Transistors

It is well known that single-wall carbon nanotubes (SWCNTs) are equivalent to rolled-up monolayer graphene sheets. Unlike graphene sheets, single-wall carbon nanotubes (SWCNTs) can be semiconducting or metallic depending on its chirality (Angle along which they are rolled-up). Since single-wall carbon nanotubes are fundamentally fascinating 1D system, and they can be explored with our QTSE platform, we expand our theoretical model to SWCNTs.

(a) (b)

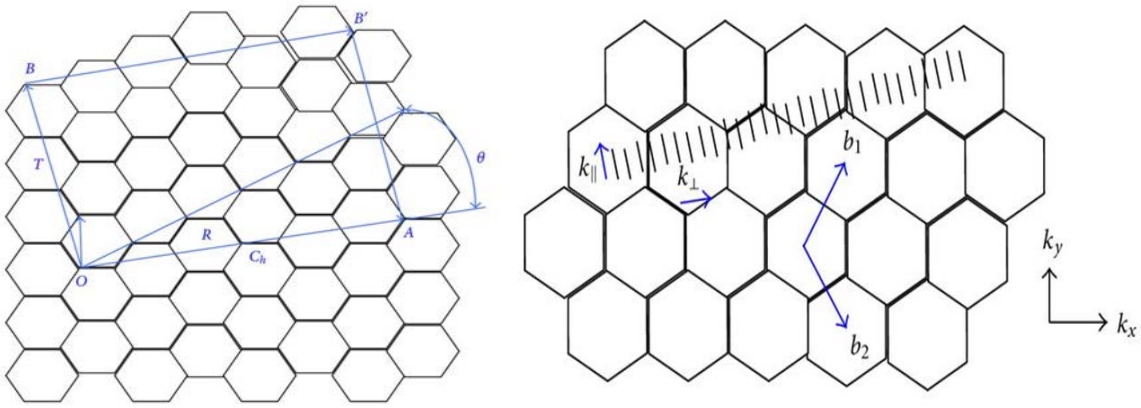

Figure 2.6: Wrapping graphene into a nanotube.(a) Definitions of vectors used to describe SWCNTs. (b) SWCNT Reciprocal lattice. Each black line represents one SWCNT transmission mode. Figure reproduced from [53].

Compared to graphene devices, one major difference is that SWCNTs have a periodic the boundary condition. Here, we present the steps to obtain, and incorporate the boundary condition into the model for SWCNTs.

First, as shown in Fig. 2.6(a), we define vectors on the graphene lattice, where $\vec{C}_h$ is the chirality (relate to the circumference of SWCNT) vector, $\vec{T}$ is the translational vector. The graphene sheet roll up in the direction of $\vec{C}_h$, and the charge carriers move along the direction of $\vec{T}$. $\vec{C}_h$ can be express as:

$$\vec{C}_h = n\vec{a}_1 + m\vec{a}_2 \tag{2.9}$$

Where n and m are two integers and define carbon nanotube indices, While $\vec{a}_1$ and $\vec{a}_2$ are unit vectors of the graphene lattice.

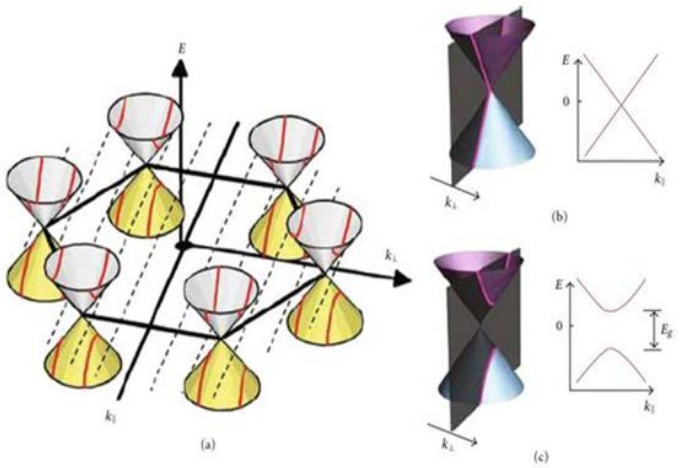

Figure 2.7: SWCNT band structure. (a)The 1D band structure of a SWCNT is given by one-dimensional cuts of the 2D graphene dispersion. (b)For a metallic SWCNT and (c)for a semiconducting SWCNT. Figure reproduced from [53]

The translational vector $\vec{T}$ can be express as:

$$\vec{T} = \frac{2m+n}{d_R}\vec{a}_1 - \frac{2n+m}{d_R}\vec{a}_2 \tag{2.10}$$

Where d_R is the greatest common divisor(GCD) of $(2m+n)$ and $(m+2n)$.

Figure. 2.6(b) shows the reciprocal lattice of graphene. The directions $\vec{k}_\perp$ and $\vec{k}_\parallel$ are the reciprocal axes related to $\vec{C}_h$ and $\vec{T}$. The black lines parallel to the $\vec{k}_\parallel$ represent the quantized transmission modes. If these allowed momentum lines pass through K points, it will lead to a metallic SWCNT without a bandgap, as shown in Fig. 2.7 (b). If these transimission modes do not match a K point, there will be a bandgap. Corresponding to a semiconducting tube, as shown in Fig. 2.7(c).

Now we are ready to define the boundary condition for SWCNTs. While in the $\vec{k}_\parallel$ direction, we match the wavefunction at each potential step, in the $\vec{k}_\perp$ direction we have:

$$\vec{C}_h \cdot \vec{k}_\perp = 2\pi N \tag{2.11a}$$

$$\vec{T} \cdot \vec{k}_\perp = 0 \tag{2.11b}$$

Since our model for graphene was written in the x, y basis, we must write Eq. 2.11 in the x, y basis as well:

$$\left(n \begin{bmatrix} \frac{1}{2}a \\ \frac{\sqrt{3}}{2}a \end{bmatrix} + m \begin{bmatrix} -\frac{1}{2}a \\ \frac{\sqrt{3}}{2}a \end{bmatrix} \right) \cdot \begin{bmatrix} k_{\perp,x} \\ k_{\perp,y} \end{bmatrix} = 2\pi N \tag{2.12a}$$

$$\left(\frac{2m+n}{d_R} \begin{bmatrix} \frac{1}{2}a \\ \frac{\sqrt{3}}{2}a \end{bmatrix} - \frac{m+2n}{d_R} \begin{bmatrix} -\frac{1}{2}a \\ \frac{\sqrt{3}}{2}a \end{bmatrix} \right) \cdot \begin{bmatrix} k_{\perp,x} \\ k_{\perp,y} \end{bmatrix} = 0 \tag{2.12b}$$

Solving the above equations for $k_{\perp,x} \neq 0$ and $k_{\perp,y} \neq 0$, we obtain the boundary condition. We note that each combination of $[n, m]$ will result in a unique boundary condition for $\vec{k}_\perp$, Where $\vec{k}_\perp$ is given by:

$$|\vec{k}_\perp| = \sqrt{{k_{\perp,x}}^2 + {k_{\perp,y}}^2} \tag{2.13}$$

In Fig. 2.2, we plot two calculated $\sigma - V_{textG}$ in respectively a $[5, 5]$ armchair SWCNT and a $[18, 0]$ Zigzag SWCNT, under various strains. Both of the tube are metallic, therefore they dont have bandgap at 0% strain, where their conductance is $\frac{4e^2}{h}$ due to their 2 spin and 2 valley degeneracies. When strain is applied, a bandgap is opened for the Zigzag tube, but no for the armchair tube. These predictions for the sizes of bandgaps(0.2eV at 3% strain), and the value of σ agree with previous experimental and theoretical studies [54,55]. Therefore, we have successfully integrated the SWCNT boundary condition into our applied QTSE model. Many technical details and explorations remain to be done, to fully explore SWCNT calculations, and this is pursued by Linxiang Huang.

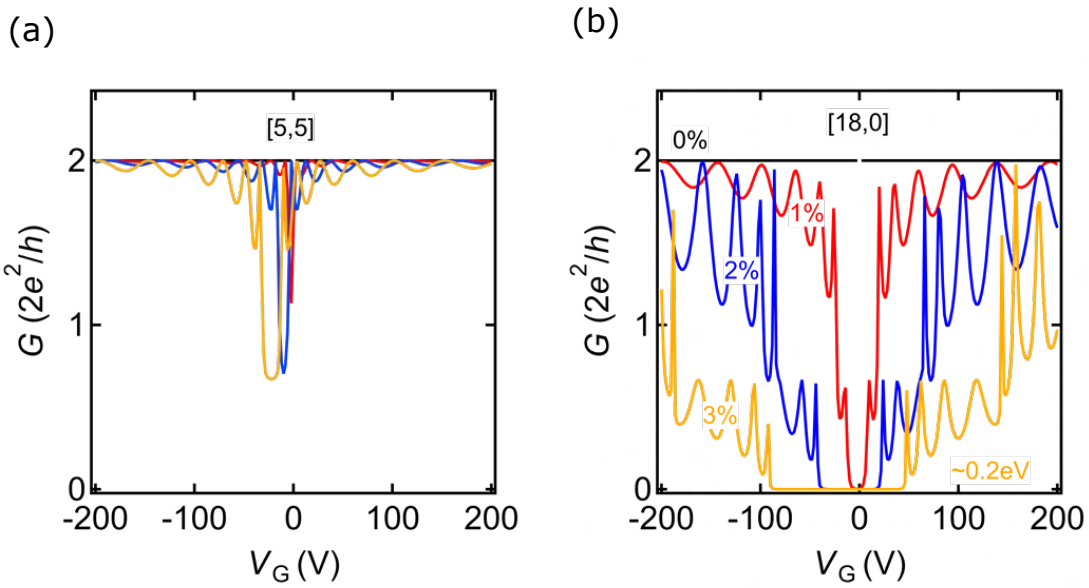

Figure 2.8: GTSE calculations in SWCNTs. $\sigma - V_{textG}$ data plotted for 2 type of SWCNT, at different strain, black curve for 0%, red curve for 1%, blue for 2%, and yellow for 3%.(a) In a $[5, 5]$ armchair SWCNT. No bandgap open when strain applied.(b) $[18, 0]$ Zigzag SWCNT, bandgap is opened when strain applied, which is about 0.2eV at 3% strain.

Chapter 3

Device Fabrication for Graphene Quantum Strain Transistors (GQSTs)

This chapter describes the methods we used to fabricate suspended monolayer graphene transistors suited for GQST. As mentioned in Chapter 2, whether the current in a GQST device can be turn off or not depends on the crystal orientation of the channel, which is difficult verify at the microfabrication stage. However, even in devices where a full suppression of conductivity is not possible, we could study the effects of strain on quantum transport. The Fabrication methods we used are based on previous methods [17] for graphene/carbon nanotube NEMS. For the next stages of this GQST project, we decided to reduced the distance between the suspended channel and the gate (substrate) to increase gating efficiency (tunability of Fermi level). In order to do so, I made several original optimizations to enable this fabrication. After fabrication, our devices will be loaded into a complex instrument for transport measurements. The instrumentation was build by A.C. McRae, thus, we will only give a brief review of the instrumentation in a following section, for more detail please refer to his thesis [17].

3.1 Wafer Preparation

Like many others who study 2DMs and transistors, we fabricate our devices on silicon wafers. As discussed in Chapter 2, to achieve graphene quantum strain

transistors(GQSTs), we proposed a platform which applies a mechanically-tunable strain by bending the silicon substrate. Therefore, to avoid shattering of the chips, we use thin wafers which are more flexible. The wafers we chose are 4", $\langle 1\,0\,0 \rangle$, heavily doped Si^- wafers with a thickness $t = 200$ μm and covered with a layer of SiO_2 on both side. We use doped silicon because it will be used as the gate electrode of the transistor, so it must remain conductive even at low temperature. We only need a SiO_2 layer on one side of the wafer, but it is grown on both sides via a thermal process. The thickness of oxide t_{ox} is 300 nm or 150 nm as purchased from the manufacturer. 150 nm oxide layer will provide a smaller channel gate spacing for better gating efficiency.

When graphene deposited on 150 nm silicon dioxide is not visible under an optical microscope. Thus we have to etch the SiO_2 to 90 nm [56]. For our 160 nm-SiO_2 wafers, we don't have to etch the SiO_2 on their backside, as the gate electrode can be deposited on the front side. For 300 nm-SiO_2 wafers, we have to remove the SiO_2 completely from their backside to connect to the gate. To do so, we use reactive-ion etching (RIE).

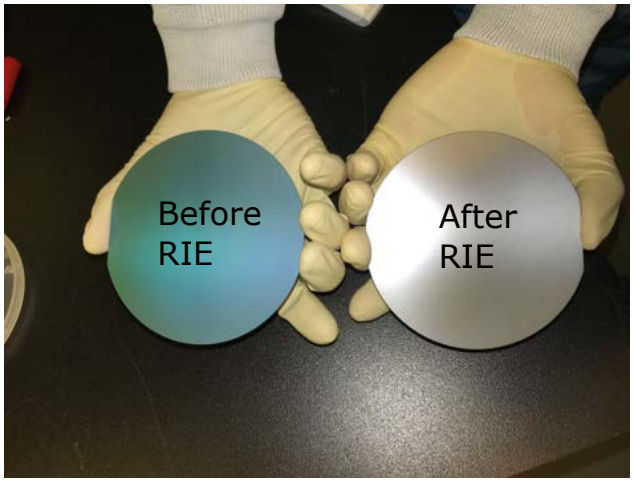

Figure 3.1: Backside wafer etching for gate contacting. The SiO_2 film is removed from the wafer's backside using a CHF_3 plasma RIE.

RIE is a dry etching method in which we use radio frequency (RF) power to generate a plasma. The ionized gases is accelerated to strike the material on the surface of samples. Depending on the chemical composition of the gases used and the material, it results in directional (anisotropic) etching of thin films. In our case, we use this method to etch SiO_2 using the following recipe. After loading a wafer in the chamber, we flow 4.5 standard cubic centimetres per minute (SCCM) of CHF_3 and

0.5 SCCM of O_2 at a chamber pressure of 125 mTorr. We then apply 300 W of RF power for 15 minutes. After etching, we measure the SiO_2 thickness by ellipsometry or reflectometry. The SiO_2 etching can be observed visually, as shown in Fig. 3.1.

We then use deep reactive-ion etching (DRIE) to etch the front side of the wafer. This is simply because among the etching instruments we can access, the DRIE instrument is the most modern tool and gives the most precise control. The oxide thickness we leave on the front side of the wafer will determine the gate-channel spacing in our transistors. The DRIE recipe is as follows: First, we flow 100 SCCM of O_2 for 3 minutes to flush the chamber. Then we set the temperature to 20°, and flow 6 SCCM of SF_6 at a chamber pressure of 25 mTorr, and apply a RF power of 50 W for 1 minute. This etches the SiO_2 from 160 nm to $\approx$ 87 nm, as measured by reflectometry.

In the final step of the initial wafer preparation, we transfer gold coordinate grids on the wafers using photolithography, as shown in Fig. 3.2. We use the same recipe as previously done in the our research group, the details can be found Ref. [17].

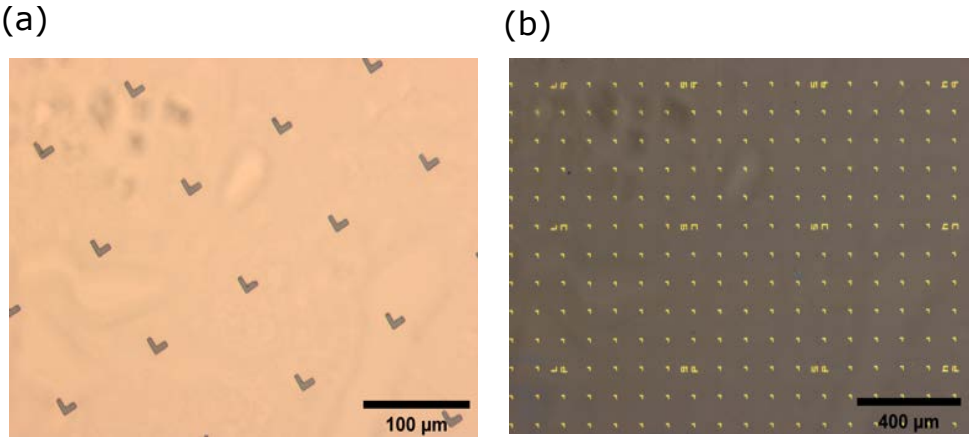

Figure 3.2: Transfer of alignment grids using photolithography and metal evaporation on the wafers. (a) Optical image of the developed grid pattern. (b) Optical microscope image of a section of the alignment grid pattern after metal deposition and lift-off procedure.

3.2 Microfabrication of Suspended Graphene Field-effect Transistors

Our suspended grapehene devices require 3 steps of fabrication [17]: First, we exfoliate monolayer graphene crystals on SiO_2/Si wafers with gold coordinate grids (see Fig. 3.2). Secondly, we transfer source and drain electrodes by electron-beam lithography and metal deposition. Thirdly, we suspended the graphene crystal via wet-etching the SiO_2 film and critical point drying.

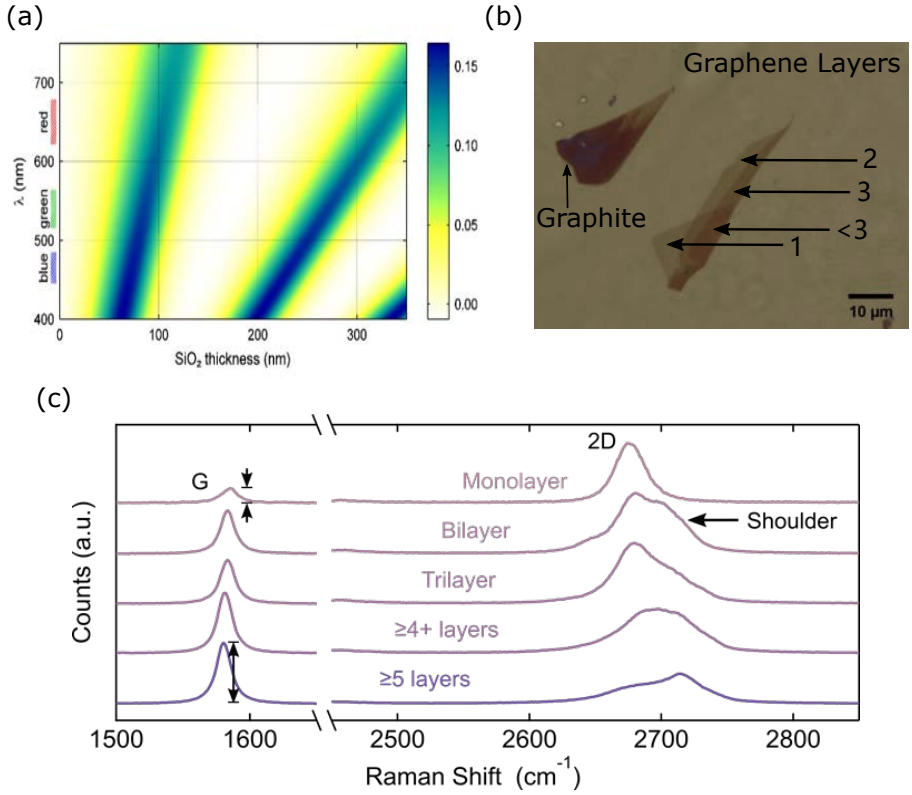

Figure 3.3: Graphene crystal exfoliation and Raman spectroscopy. (a) Contrast visible light of graphene on SiO_2 versus wavelength and SiO_2 thickness. To maximize contrast, we etch the SiO_2 layer to 90 nm. panel (a) was reproduced from a paper by P.Blake et al. [56]. (b) Optical image of exfoliated graphene/graphite of various thickness. (c) Normalized and vertically offset Raman spectra for many thickness of graphene taken from the locations shown in panel (b), showing the evolution of the G and 2D peaks with the number of layers. panel (c) reproduced from [17].

In step 1, we use a mechanical exfoliation (also called "Scotch Tape Method"), where Highly-ordered pyrolitic graphite is exfoliated (cleaving atomic planes along

the c-axis of graphite) using an adhesive tape repeatedly, and then pressed on the substrate. The detailed procedure can be found in [57]. After exfoliation, we locate and identify tye large and isolated monolayer graphene crystals via optical microscopy and Raman spectroscopy. Light reflection (contrast) is proportional to the numbers of graphene layers and also dependeds on the SiO_2 thickness (see Fig. 3.3(a)). We can roughly determine the number of layers by optical microscope, and record the exact location of the crystal on the substrate. Then, we use Raman spectroscopy [58] to decisely determine the number of layers as shown in Fig. 3.3(c).

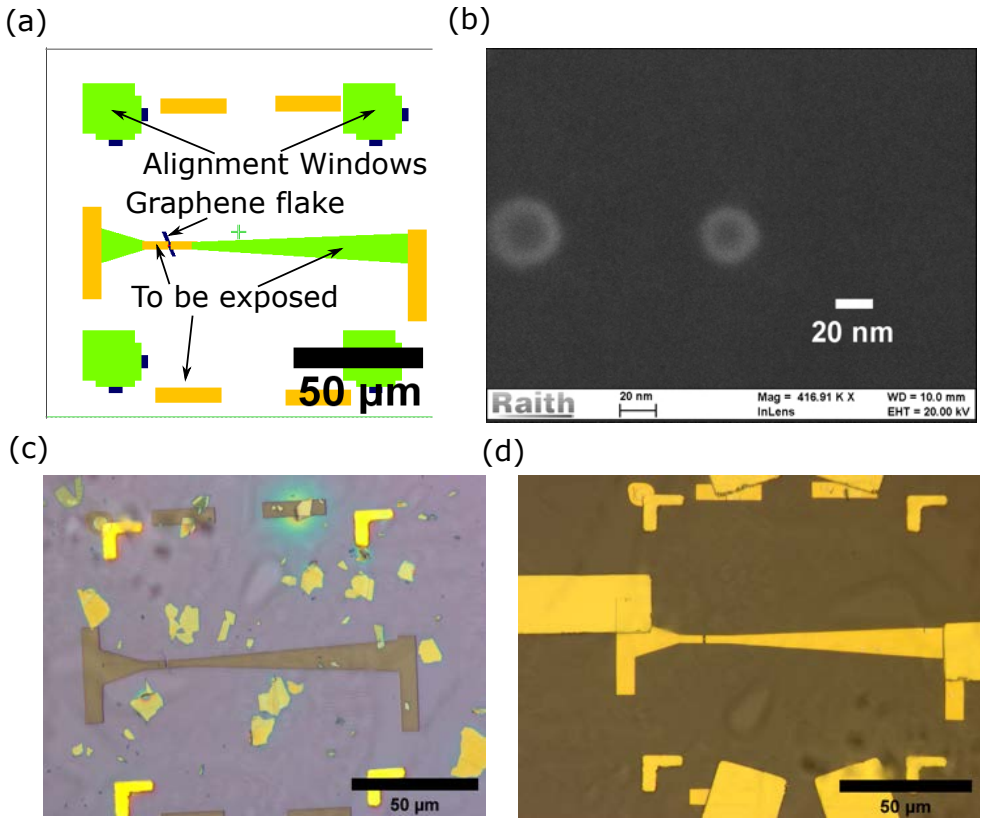

Figure 3.4: Four key stages of the microfabrication of GQST devices. (a) CAD design of gold-on-graphene junctions. The square windows at the corners are used to align the CAD design to the crystal during patterning. (b) Exposed resolution-test dot near the designed pattern. A circular dot with a diameter of 20 nm indicates correct focus settings of the EBL. (c) Optical image of a GGJ device after EBL exposure and development. (d) Optical image of the final state of a GGJ device, after metal evaporation, liftoff and suspension.

In step 2, we use d-beam lithography (EBL) to define electrodes. We begin the EBL process by spin coating the chips with PMMA (Poly methyl methacrylate) resist.

We spin the chip with 3000 RPM for 1 minute, which results in a uniform layer with a thickness of 200 nm. Then we bake the chip on a hot plate at 170° C for 15 minutes. Using a computer-aided design (CAD) software, we create a map of the positions of the crystals on the chip and design electrodes contacting the crystals. As shown in Fig. 3.4(a), we distinguish areas needing exposure or not and assign different electron charge doses to different areas. The doses are determine by a dose (exposure) test normally run before the actual exposure. We choose the doses which give sharp lithographic edges but which allow for modest variations without compromising the integrity of the lithography. Once the CAD file is ready, we load our sample in the EBL system. To achieve a precise and reproducible exposure, we adjust carefully the focus and stigmation of the electron beam and verify that a "test" dot exposed near the desired region has a diameter as small as 20 nm, as shown in Fig. 3.4(b). The symmetry of the dot is determined by the a stigmation accuracy, while the sharpness is determined by the focus precision. We expose our CAD pattern using a 10 μm aperture, 20 kV acceleration voltage and a 10 mm working distance. We use 666 magnification so that the entire exposure region is within one write field of the EBL.

After the exposure, we use MIBK (methyl isobutyl ketone) to develop the exposed resist. Specifically, we mix a solution of 1:3 MIBK:IPA (isopropyl acetate) in which we develop our chips for 30 seconds, and we rinse the sample in IPA. In Fig. 3.4(c), we show an optical image of a sample after development, where we see the exposed pattern. After development, we deposit 60 nm of gold using thermal evaporation [17]. Than we perform a liftoff of the unexposed PMMA resist in warm acetone, which removes the metal everywhere excepts in exposed area, as shown in Fig. 3.4(d).

The two types of devices we designed for GTSE experiments are graphene-under-gold break-junctions (GAuBJs), shown in Fig. 3.5(a)(b), and graphene gap-junctions (GGJs), shown in Fig. 3.5(c)(d). The GAuBJs can also be modified for CNTs, 2DMs, or even just pure gold. They are aimed channels with narrow dimension, such as quantum dots. GGJs are designed for GQSTs. Fig. 3.5(b)(d) are top-down views of SEM images of a GAuBJ and a GGJ respectively, which I have fabricated.

In step 3, we use a buffered oxide etch (BOE) to remove SiO_2 under the graphene channel and suspend it. We use a 49% HF, and mix it 1:7 with a buffer solution of NH_4F. We measured a etch rate of 70 nm/min by reflectometry measurement. After calibration of the etch rate, we etch the desired SiO_2 thickness. We then rinse our

sample in DI water to stop the etch, and then transfer the sample in IPA. Since a liquid's surface tension can cause thin suspended devices to collapse as they dry, we dry the sample using a critical point dryer. Fig. 3.4(d) shows a GGJ device after microfabrication. Because the SiO_2 was etched, we see a different substrate color than in Fig. 3.4(c).

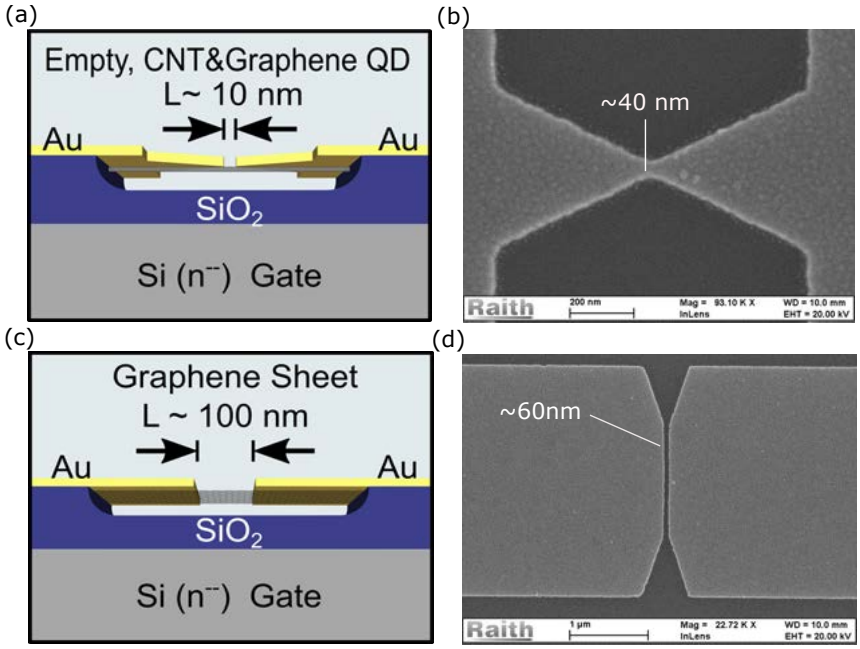

Figure 3.5: Designed device geometery and their SEM images after fabracation. (a) A diagram of AuBJ.(b) A SEM image of AuBJ, where we achieve a channel width of 40nm. (c) A doagra, pf AuGJ.(d) A SEM iamge of AuGJ, where we achieve a channel length of 60nm.

After microfabrication, we wire-bond our sample to a chip holder, as shown in Fig. 3.6. Then we load the sample holder in our system build for QTSE experiments. The detail of this system and how our instrumentation functions can be found in [17]. Briefly, as shown in Fig. 3.7, it is a platform where we use a high precision computer-controlled screw assembly to bend the Si substrate. The bottom part of the probe, where our sample is located, will be inserted into a low-temperature cryostat that allow us to do quantum transport measurements.

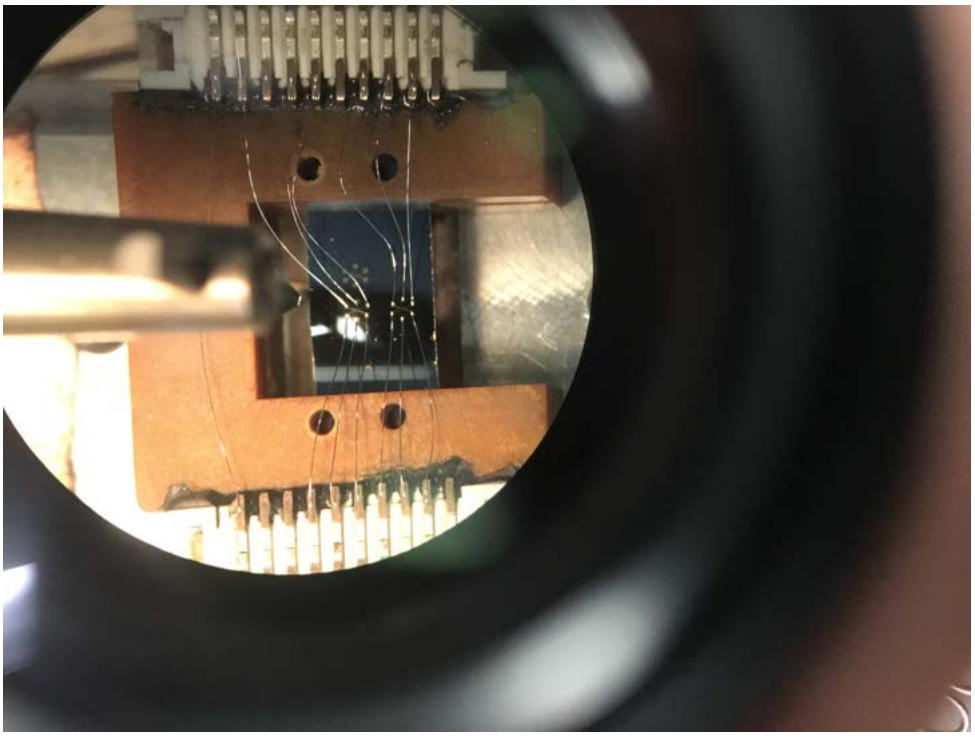

Figure 3.6: Wire Bonding. We wire up contact pads on the wafer to the sample holder, which allow us to do transport measurement.

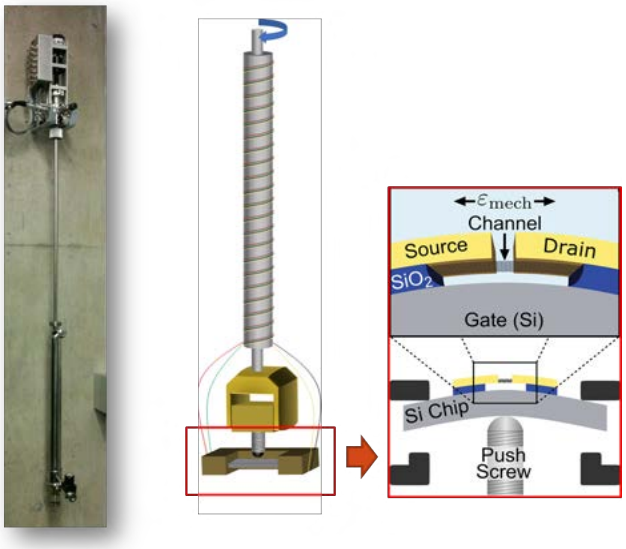

Figure 3.7: QTSE instrumentation. Left, the photo of measurement probe. Middle, the diagram of measurement probe. Right, the diagram of the chip holder and device.

3.3 Different Type of Devices Fabricated for Other Projects

Besides the devices I have fabricated for the GQST project, I have also fabricated devices for other projects. Shown in Fig. 3.8(a) is a suspended bilayer graphene device, designed for the study of bilayer graphene electromechanical resonators. It was made for my colleague Wyatt Wright, and has not been studied yet. Figure. 3.8(b) is a graphene transistor on SiO_2/Si substrate. The large dimensions of the channel was designed for photocurrent measurements. This device has been studied and reported in Gareth Melin's thesis [59]. These devices were fabricated differently with EBL using a 60 μm aperture, 10 kV acceleration voltage, and 10 mm working distance. The fabrication details can be found elsewhere [59].

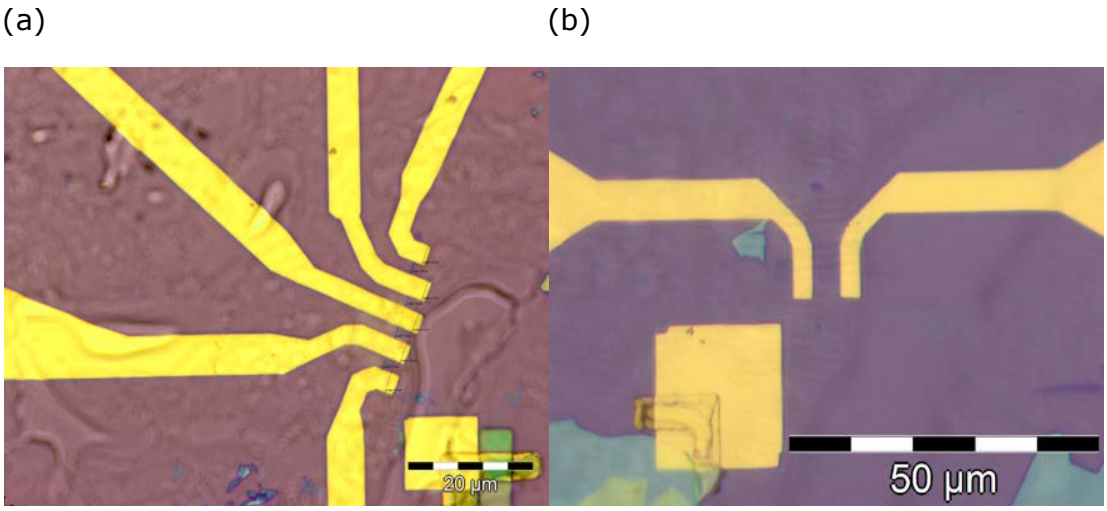

Figure 3.8: Different type of devices fabricated for other projects. (a) Optical image of doubly clamped bilayer graphene resonators, this type of device is used for AC measurement to study electromechanical resonances in bilayer Graphene. (b) Optical image of a graphene transistor with a large channel dimension for the study of photocurrent generation.

Chapter 4

Experimental Graphene Transport Strain Engineering (GTSE)

This chapter reports a graphene transport strain engineering (GTSE) experiment performed with the platform described in the previous chapters. In this experiment, we study the effects of strain-induced scalar potentials, $\Delta\mu_\varepsilon$, and vector potentials, $\boldsymbol{A}$, on transport respectively. We observed these effects by measuring the charge conductance through a suspended graphene channel at different strains and gate voltages, while holding bias voltage at 0.5 mV and temperature at 0.3 K. This device was fabricated and measured by my colleague Andrew McRae; the detailed fabrication procedure and characterization of this device can be found in his thesis [17]. My main contribution to this experiment is the detailed and extensive data analysis, where I have extracted physical quantities and compared the results to previous theory [10], and our model [1]. The analysis showed in this chapter represents a publication that is currently in preparation, and where I will be the co-first author.

In this Chapter, we first describe the device we measured and the measurement method. Then, we present the data analysis of the experimental data shown in Fig. 4.1. We begin by calculating experimental parameters for this device, such as the applied mechanical strain. In some cases, we derive equations to fit our data in order to extract microscopic information about the device, e.g. its crystal orientation. We experimentally observe the strain-induced scalar and vector potentials, which were predicted in our theoretical model. We show that by inserting all of the extracted parameters into our model, we can accurately reproduce the experimental data without

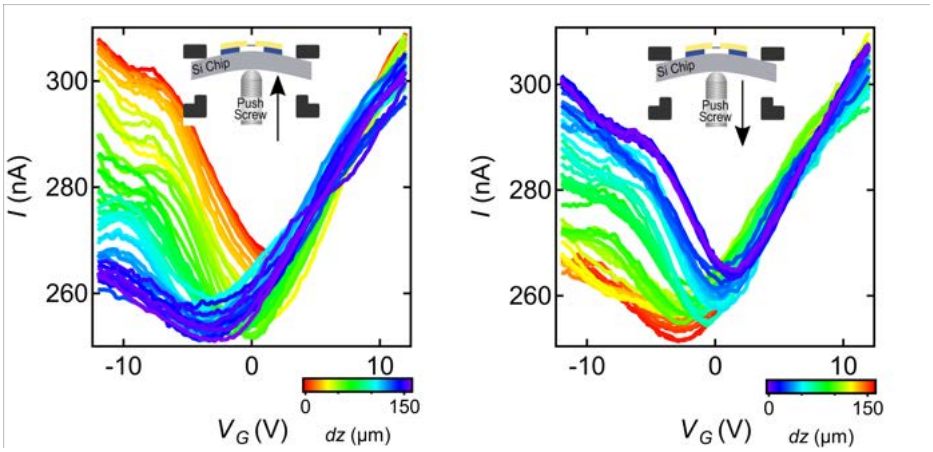

Figure 4.1: Main experimental data set, $I - V_G - \varepsilon_{\text{mech}}$ data taken at $V_B = 0.5$ mV $T = 0.3$ K. (a) and (b) show the forward and reverse motion of the mechanical sweep.

any free parameter. We demonstrate that we can tailor the energy level, electron transport and quantum interferences of graphene QNEMS.

4.1 Device Characterization and Measurement Method

As shown in Fig. 4.2, We studied a field-effect transistor (FET) device with a suspended graphene channel of $L = 90 \pm 10$ nm, $W = 600 \pm 20$ nm and cantilever arm with suspension length of $u = 700 \pm 50$ nm. The suspension height and oxide thickness are $t_{\text{vac}} = 211$ nm and $t_{\text{ox}} = 106$ nm, respectively, as measured by reflectometry and ellipsometry. This device was fabricated using the procedure reported in Chapter 3, and the exact fabrication details can be found in [17].

Before the charge transport measurements, we clean this device in high vacuum inside the measurement cryostat via Joule heating (annealing). This is an important step because fabrication leaves residues on the graphene, which introduce charge impurities that affect transport. When current annealing, we heat the suspended channel to remove residues and water [60, 61]. To anneal our samples, we used the circuit shown in Fig. 4.3, and applied a power of 1.3 mW for 10 minutes. Afterwards, we performed DC transport measurements using the circuit shown in Fig. 4.4. We used a computer-controlled data acquisition card (DAQ) to apply a bias voltage through a voltage divider. We used a Keithley 2400 voltage supply to apply voltages to our

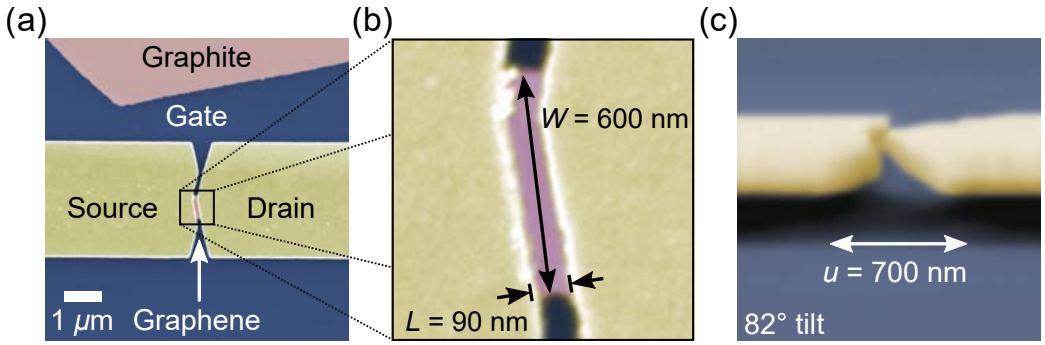

Figure 4.2: False colour SEM images of the measured suspended graphene FET. (a) SEM image of the device, showing the Au films (yellow) covering the graphene source and drain electrodes, the back gate which is under the oxide (blue), and the graphene channel (pink). (b) Close-up view of the channel. (c) Tilted-SEM image of the device, taken at 82° tilt, clearly showing the suspension and undercut length. This figure was reproduced from [17].

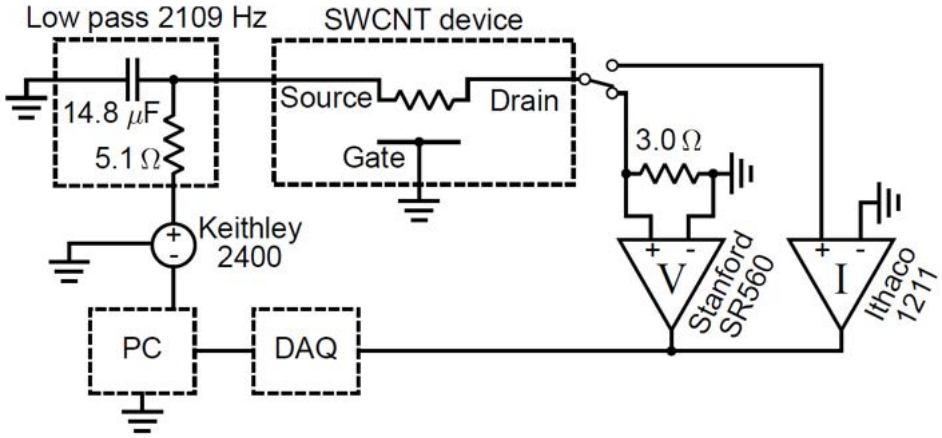

Figure 4.3: Current annealing circuit. A feedback system controls the voltage applied to the device by constantly measuring the resistance of the device. This figure was reproduced from [17].

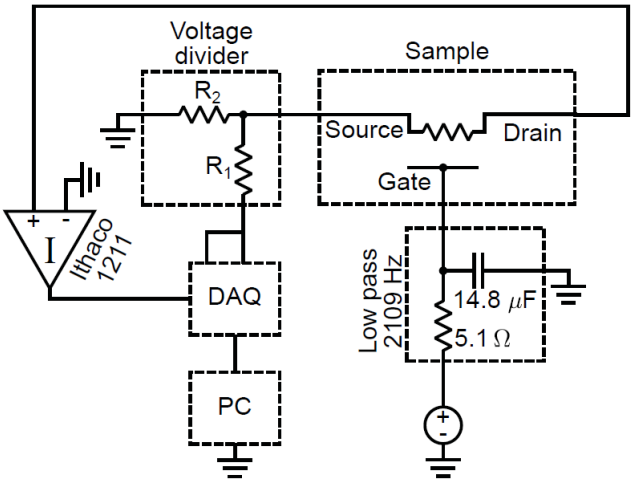

Figure 4.4: DC charge transport measurement circuit optimized for low-noise measurements of current as a function of bias and gate voltages. This figure was reproduced from [17].

sample's gate electrode through a low-pass filter, which prevents voltage spikes. We measured the current at the drain electrode via an Ithaco 1211 current preamp and sent the output to the DAQ.

For charge transport data acquisition, we measured current flow in our samples versus V_G from -12V to +12V, and at 52 different motor positions, where the maximum displacement of the screw was 160 μm. The bias voltage was set to 0.5mV, the temperature to 0.3K. We stopped the annealing when we saw a clear current minimum in the $I - V_G$ curve, reflecting a clearly defined Dirac point in graphene. In Fig. 4.5, we show examples of these measurements taken for different anneal steps. We used the data taken after Anneal #15 as our final raw data set for the data analysis. We present both the forward and reverse mechanical sweeps data in Fig. 4.1 to show the reproducibility of our measurement method and sample.

During measurements, we noticed that the first time we stretched the channel some minor but permanent changes to the microscopic mechanical configuration of the suspended crystal took place. Therefore, the first mechanical sweep data following a new annealing was not analyzed in detail since it is less reproducible than the following mechanical sweeps. Data where the current was less than 0.01 pA were not analyzed due to their low signal-to noise ratio. Transport measurements taken at intermediate (not final) annealing stages were not analyzed since the device was still highly disordered.

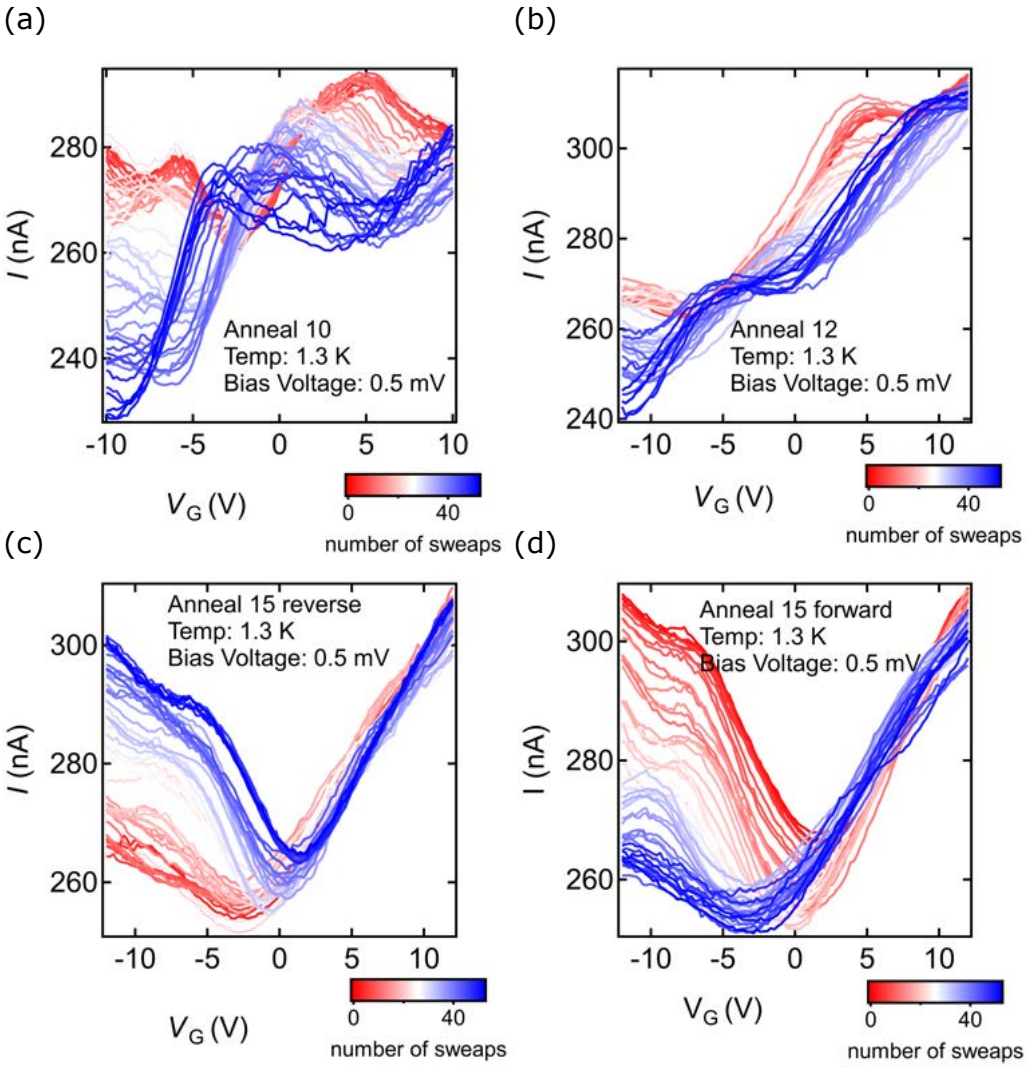

Figure 4.5: $I - V_G - \varepsilon$ data from the suspended graphene FET measured at various annealing stages. (a) Data taken after Anneal #10. (b) Data taken after Anneal #12. (c) Forward-strain sweep data after Anneal #15. (d) Reverse-strain sweep data after Anneal #15.

4.2 Calibration of the Applied Mechanical Strain

Finding the exact relationship between the displacement of the push screw instrumentation (dz) and the microscopic channel stretching (dx) is crucial for our experiment. Ideally, it would follow [40]:

$$dx = \frac{3ut}{D^2} dz \tag{4.1}$$

Where D is the distance of the chip clamps, t is the chip thickness, and u is the total undercut length; these quantities were labelled in Fig. 2.1 and Fig. 4.2. A much more reliable estimate can be done by fitting the data from gold tunnel junctions on the same chip measured with our instrumentation.

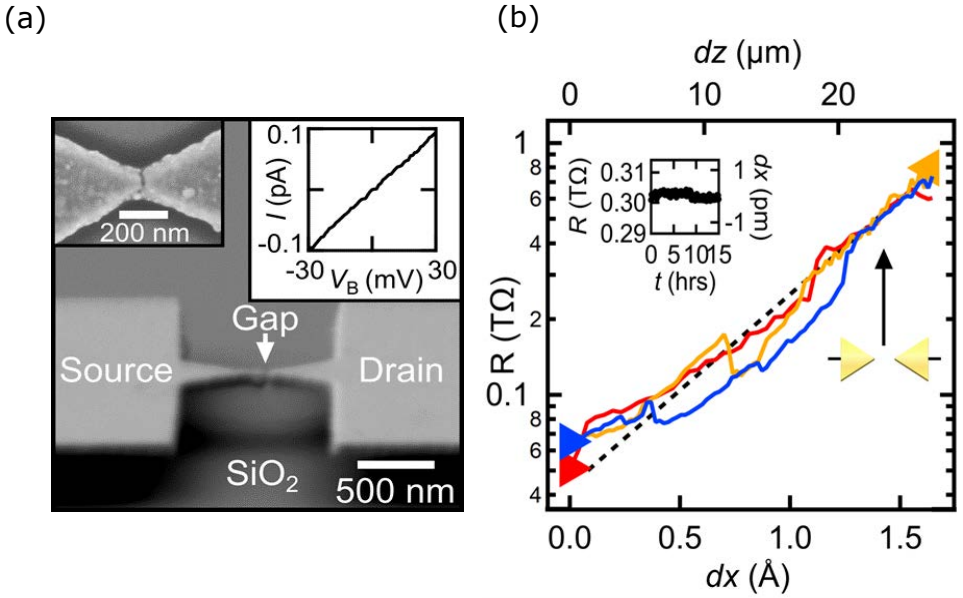

Figure 4.6: Calibration via gold tunnel junctions. (a) Tilted-SEM image of a gold tunnel junction. A gap with few nanometer length in the middle of the channel is opened by electromigration. (b) Three measurements showing log plot of the resistance of the gold tunnel junctions vs. strain. The red and blue curve are forward-strain measurement. The yellow is reverse-strain measurement. The inset shows the measurement of resistance vs. time.

Electromigration of the gold break junction, as shown in Fig. 4.6(a), creates a gap tunnel junction in the gold wire whose width is of a few nanometers. When the gap is

stretched precisely the tunnel junction resistance is:

$$R \propto e^{2\kappa x}, \kappa = \frac{\sqrt{2m_e\phi_{Au}}}{\hbar} \approx 1.18 \times 10^{10} m^{-1} \tag{4.2}$$

Where $m_e = 511$ keV$/c^2$ is the electron mass, and $\phi_{Au} \approx 5.3$ eV is the work function of gold. By fitting R/R_0 vs dz in the linear regime of the data shown in Fig. 4.6(b), we obtained:

	dx/dz
AuBJ1	$(6.1 \pm 0.3) \times 10^{-6}$
AuBJ2	$(5.7 \pm 0.3) \times 10^{-6}$
AuBJ3	$(7.7 \pm 0.3) \times 10^{-6}$
AuBJ4	$(4.6 \pm 0.3) \times 10^{-6}$

Table 1: dx/dz value measured from four gold tunnel junction experiments.

In table. 1, we show the dx/dz calibration from four gold tunnel junctions. We use the average dx/dz value in the rest of our data analysis. Moreover, we are able to verify the accuracy of this calibration *in situ*, inside our graphene device, as explained below.

All our device were fabricated on the same batch of wafers and measured using the same instrumentation, which means that the suspended graphene FET shown in Fig. 4.2 and the four gold tunnel junctions we studied have the same substrate thickness and chip clamping distance. Therefore, according to Eq. 4.1, the only parameter causing dx/dz to differ from device to device is the gold cantilever suspension length, u. Thus:

$$\frac{dx_{AuBJ}/dz_{AuBJ}}{dx_{device}/dz_{device}} = \frac{u_{AuBJ}}{u_{device}} \tag{4.3}$$

According to Fig. 4.2, our device has a suspension length $u = 700 \pm 100$ nm and a channel length $L = 90 \pm 10$ nm. For a range of screw displacement of $dz_{\max} = 160 \pm 10$ μm, we find $dx_{\max} = 7.5 \pm 1.5$ Å. Thus, our maximum mechanical strain applied is $\varepsilon_{\text{mech}} = 0.8 \pm 0.2\%$.

Our motor drives the push screw via a long and complex mechanical assembly. It should not be surprise that there is a delay between the screw motion and motor rotation, as the transmission rod can slightly twist before driving the screw. Mechanical hysteresis occurs when we switch from forward motion to reverse motion. We

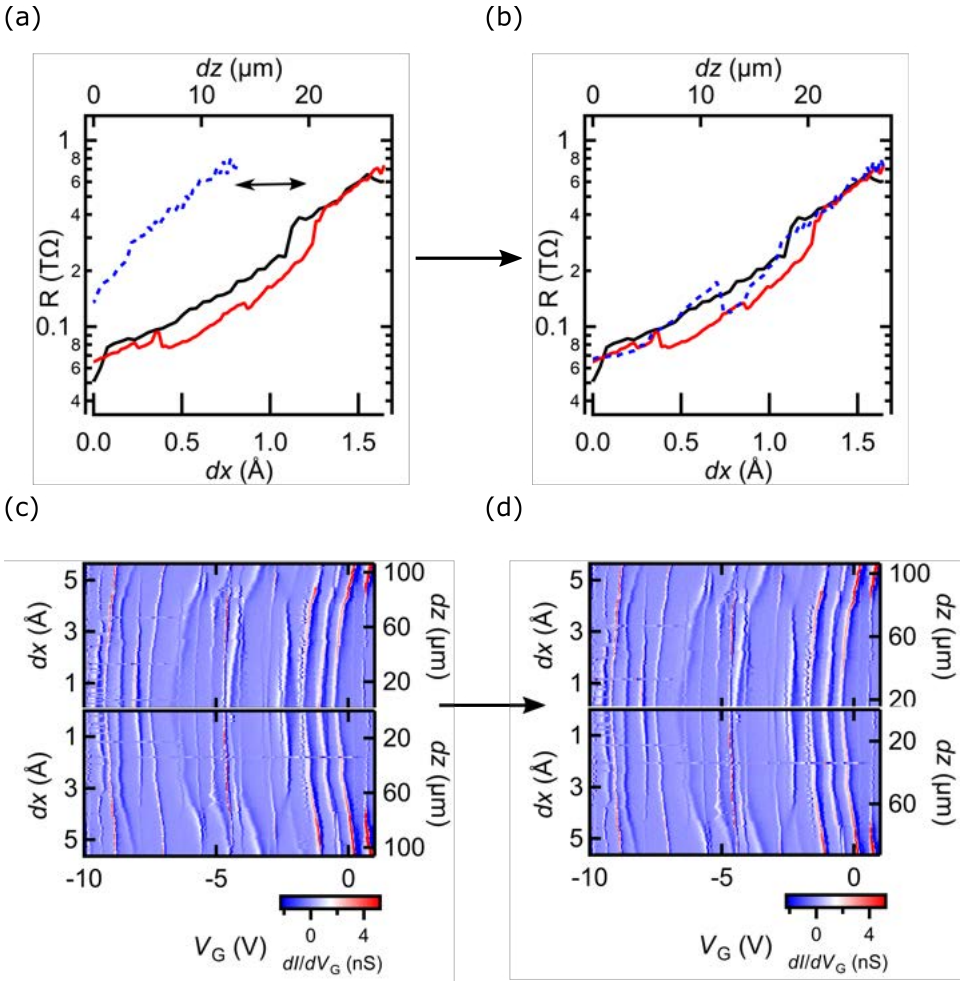

Figure 4.7: Determination of the instrumentation's mechanical hysteresis. (a)-(b) Align the forward and reverse resistance data for a gold tunnel junction. (c)-(d) Align the positions and symmetry of conductance resonance.

measured this mechanical hysteresis by comparing the $R - dx$ data between a rigid and reproducible shift of forward and reverse data sweeps. We found the mechanical hysteresis to be $dz = 14 \pm 1$ μm, $dx = 0.9 \pm 0.1$ Å. This mechanical hysteresis is shown in Fig. 4.7. In Fig. 4.7(a), we show forward (black and red) and reverse (blue) sweep data for a gold tunnel junction. In Fig. 4.7(b), we show that when we apply a $dz = 14 \pm 1$ μm shift, the forward data and the reverse data lay accurately on top of each other. In Fig. 4.7(c), we show $dI/dV_G - V_G - dx$ data for a graphene quantum dot (QD) device measured in this instrumentation reported in [17], where the forward data is at the top and the reverse mechanical sweep is at the bottom. In Fig. 4.7(d), we show after we apply $dz = 14 \pm 1$ μm shift, the conductance resonance peaks (from eigenstates on the QD) align precisely. Fig. 4.7(d) have better top and down symmetry than Fig. 4.7(c). Also, by comparing the forward-strain and reverse-strain fully reproducible data in Fig. 4.7 (c)–(d), we can conclude there is no slippage for our devices under our instrumentation. The graphene is well-clamped with the gold cantilever and hence all $\varepsilon_{\text{mech}}$ is applied to the channel.

4.3 Measurement of the Strain-Induced Scalar Potential

In the main dataset shown in Fig. 4.1, we see a clear shift of the Dirac point V_{D}, which is caused by the strain-induced scalar potential. This V_{D} shift is predicted by Eq. 2.8. Since we performed our measurements at a constant temperature of 0.3 K, the only component changing the strain is $\varepsilon_{\text{mech}}$, and we can rewrite the equation as:

$$\Delta V_D = -\frac{e}{c_G}\frac{g_\varepsilon^2}{\pi(\hbar v_F)^2}(1-\nu)^2[(\varepsilon_{\text{mech}} + \varepsilon_{\text{thermal}})^2 - {\varepsilon_{\text{thermal}}}^2] \tag{4.4}$$

Where $\nu = 0.165$ is the Poisson ratio, g_ε is the scalar potential prefactor, $C_G = 3.7 \times 10^{-9}\text{F/cm}^2$ is the capacitance per unit area, given by Eq. 2.2. The thermal strain, $\varepsilon_{\text{thermal}}$, in the suspended graphene channels is given by Eq. 2.3, which leads to $\varepsilon_{\text{thermal}} = 1.6 \pm 0.2\%$ at $T = 0.3$ K.

Using Eq. 4.4, we fit the $\Delta V_D - \varepsilon_{\text{mech}}$ data in Fig. 4.9, as shown by the solid black lines, which gives $g_\varepsilon = 3.05 \pm 0.06$ eV. This is in good agreement with literature [50, 62, 63]. The maximum scalar potential induced by $\varepsilon_{\text{mech}}$ is $\Delta\mu_\varepsilon = g_\varepsilon(1-\nu)\varepsilon_{\text{mech}} =$

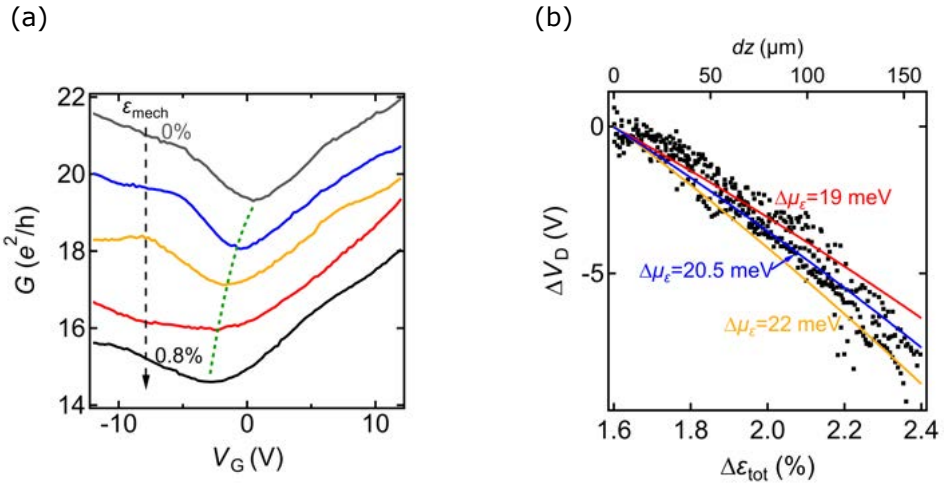

Figure 4.8: Experimental evidence of the scalar mechanical potential. (a) $G - V_G$ data at five different $\varepsilon_{\text{mech}} = 0, 0.2, 0.4, 0.6, 0.8$ % in the reverse mechanical sweep.(b) Experimental Dirac point shift data (dots) and theoretical predictions (lines) for three different maximum $\Delta\mu_\varepsilon$.

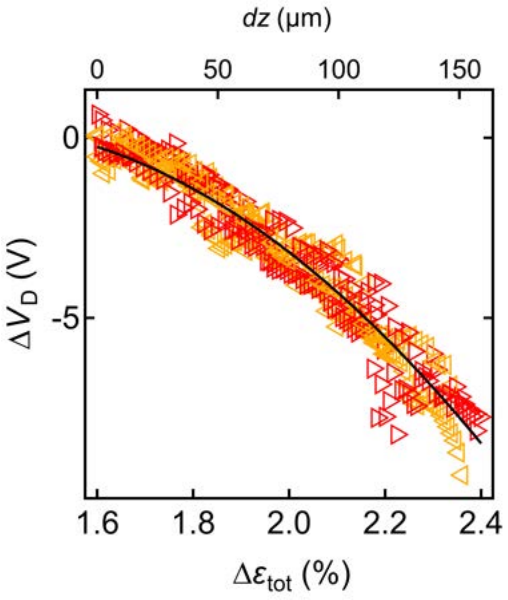

Figure 4.9: Fitting of the Dirac point data with Eq. 4.4.

20.4 ± 1.5 meV. Thus, we are able to smoothly, mechanically tune $\tilde{E}_F$ and the workfunction of graphene by over 20 meV.

4.3.1 Estimate of the Charge Impurity Density

We use this measurement of g_ε to estimate the impurity density in the graphene channel, which remains even after annealing. The Dirac point lies at $V_\mathrm{D} = 1.2 \pm 0.2$ V in the device shown in Fig. 4.2, as measured in Fig. 4.1, when $\varepsilon_\mathrm{mech} = 0$ %. Based on the thermal strain, $\varepsilon_\mathrm{thermal} = 1.6\%$, and Eq. 4.4 we calculate $V_\mathrm{D} = -4.8 \pm 0.5$ V at $\varepsilon_\mathrm{mech} = 0\%$. This discrepancy of 6V between the experimental and theoretical Dirac point value corresponds to an impurity density of $n_\mathrm{imp} = C_\mathrm{G} V_\mathrm{G}/e \approx -(1.4 \pm 0.1) \times 10^{11}$ cm^{-2}, where the minus sign indicates that the channel impurities are p-type.

4.4 Measurement of the Strain-Induced Vector Potential

In this section, we demonstrate our method to extract strain-induced vector potential by analyzing its transport signature, which is the suppression of the conductance. We first derive a fitting equation for this suppression and then we use this equation to fit the aligned data.

4.4.1 Derivation of the Conductance Fit Function

In Chapter 2, we found that the strain-induced change in the nearest-neighbour hopping energy can be incorporated in the Hamiltonian as gauge vector potentials $\boldsymbol{A}_i$ [1]. The total gauge potential in each valley K_i is $\boldsymbol{A}_i = \boldsymbol{A}_{\mathrm{lat},i} + \boldsymbol{A}_\mathrm{hop}$. Where each term is given by Eq. 2.5.

The trajectory of a charge carrier across the FET is described by the momentum wavevector in the contacts, $k_F = \pm|k\hat{x} + q_n\hat{y}|$, and in the channel, $\tilde{k}_F = \tilde{k}\hat{x} + \tilde{q}_n\hat{y}$, where $\pm$ refers to electron or hole transport, respectively. The transverse boundary condition conserves the y-momentum throughout the device, such that $\tilde{q}_n = q_n - \boldsymbol{A}_{i,y}$. The $\boldsymbol{A}_{i,y}$ shift in y-momentum alters the propagation angle of the charge carriers, and the Klein transmission probability at the strained/unstrained interfaces (where this is also a step in charge density). We solve for the transmission probability $T_{\xi,i,n}$ of

conduction mode n in valley $\xi = \pm 1, i = 1, 2, 3$. We used Eq. 2.6 and $q_n = \frac{\pi}{W}(n + \frac{1}{2})$ as the quantized transversal momentum for mode n. We calculate G across the FET by summing the transmissions from all modes:

$$G = \frac{2e^2}{h}\frac{1}{3}\sum_{\xi}\sum_{i}^{3}\sum_{n}^{N} T_{\xi,i,n} \tag{4.5}$$

where $N = \mathrm{Int}(k_F W/\pi + \frac{1}{2})$ is the number of energetically allowed modes set by the contact's Fermi energy, and the factor $\frac{1}{3}$ accounts for the lifting of the three-fold K and K' valley degeneracy in strained graphene.

In our device, while the Fermi level in the channel is tunable through $\Delta\mu_G$ and $\Delta\mu_\varepsilon$ (see Eq. 2.4), the Fermi level in the contacts is constant. Therefore we can experimentally set these two energies equal to each other at some specific $\Delta\mu_G$ and $\Delta\mu_\varepsilon$, i.e. $k_F \approx \tilde{k}_F$. The strained Fermi velocity is given by $v_x = (1 + (1-\beta)\varepsilon_{\text{total}})v_F = 0.96V_F \approx v_F$ and $v_y = (1 - (1-\beta)\nu\varepsilon_{\text{total}})V_F = 0.99v_F \approx v_F$. The Fermi wavevectors are $\tilde{k} = v_x^{-1}[\tilde{k}_F^2 - v_y^2(q_n - \xi \boldsymbol{A}_{i,y})^2]^{1/2}$, and $k = (k_F^2 - q_n^2)^{1/2}$. Finally, the transmission of a single mode is:

$$\begin{aligned}
T_{\xi,i,n} &= \frac{1}{\cos^2[\tilde{k}L] + \frac{(k_F^2 - q_n(q_n - \xi\boldsymbol{A}_{i,y}))^2}{k\tilde{k}}\sin^2[\tilde{k}L]} \\
&= \frac{1}{\cos^2[\tilde{k}L] + \frac{(k_F^2 - q_n\tilde{q}_n)^2}{k\tilde{k}}\sin^2[\tilde{k}L]} \\
&= \frac{1}{\cos^2[\tilde{k}L] + \frac{(k_F^2 - q_n\tilde{q}_n)^2}{(k_F^2 - q_n^2)(k_F^2 - \tilde{q}_n^2)}\sin^2[\tilde{k}L]} \\
&= \frac{1}{\cos^2[\tilde{k}L] + \frac{(k_F^2 - q_n^2)(k_F^2 - \tilde{q}_n^2) + k_F^2(q_n - \tilde{q}_n^2)^2}{(k_F^2 - q_n^2)(k_F^2 - \tilde{q}_n^2)}\sin^2[\tilde{k}L]} \\
&= \frac{1}{\cos^2[\tilde{k}L] + (1 + \frac{k_F^2(\xi\boldsymbol{A}_{i,y})^2}{k^2\tilde{k}^2})\sin^2[\tilde{k}L]} \\
&= \frac{1}{1 + \frac{k_F^2(\xi\boldsymbol{A}_{i,y})^2}{k^2\tilde{k}^2}\sin^2[\tilde{k}L]}
\end{aligned} \tag{4.6}$$

And the total conductance is found by introducing Eq. 4.6 to Eq. 4.5,

$$\begin{aligned} G &= \frac{2e^2}{h}\frac{1}{3}\sum_{\xi}\sum_{i}^{3}\sum_{n}^{N} T_{\xi,i,n} \\ &= \frac{2e^2}{h}\frac{1}{3}\sum_{n}^{N}(T_{1,1,n}+T_{1,2,n}+T_{1,3,n}+T_{-1,1,n}+T_{-1,2,n}+T_{-1,3,n}) \\ &= \frac{2e^2}{h}\frac{1}{3}(\sum_{n}^{N} T_{1,1,n}[q_n]+\sum_{n}^{N} T_{1,2,n}[q_n]+\sum_{n}^{N} T_{1,3,n}[q_n] \\ &\qquad +\sum_{n}^{N} T_{-1,1,n}[q_n]+\sum_{n}^{N} T_{-1,2,n}[q_n]+\sum_{n}^{N} T_{-1,3,n}[q_n]) \end{aligned} \tag{4.7}$$

When the number of channels N is large:

$$\begin{aligned} G_{\xi,i} &= \frac{e^2}{h}\frac{1}{3}\sum_{n}^{N}\frac{2k_F W}{N\pi}T_{\xi,i,n}[\frac{2k_F n}{N}-k_F] \\ &\approx \frac{e^2}{h}\frac{1}{3}W\int_{-k_F}^{k_F}\frac{d(q_n)}{\pi}T[q_n] \end{aligned} \tag{4.8}$$

For $k_F >> A_y$, $k_F L >> 1$, this reduces to [10],

$$G_{\xi,i} = \frac{e^2}{h}\frac{1}{6}W\left(\frac{4}{\pi}k_F - |\xi \boldsymbol{A}_{i,y}|\right) \tag{4.9}$$

Summing both valleys to obtain the total conductance:

$$G = \frac{2e^2}{h}\frac{1}{6}\sum_{\xi}\sum_{i}^{3}\left(\frac{4}{\pi}k_F - |\xi \boldsymbol{A}_{i,y}|\right)W \tag{4.10}$$

Eq. 4.10 can be used to fit the experimental G data and extract $\boldsymbol{A}_{i,y}$.

4.4.2 Determination of Crystal Orientation and chemical potential in the Lead $\Delta\mu_{\text{contact}}$

Two important experimental parameters are hidden in Eq. 4.10, and must be extracted from the experimental data to quantitatively compare to the model. The first one is $\theta_{crystal}$, which is a key quantity to determine $\boldsymbol{A}_{i,y}$, as per Eq. 2.5. The second is $\Delta\mu_{\text{contact}}$ which determines k_F.

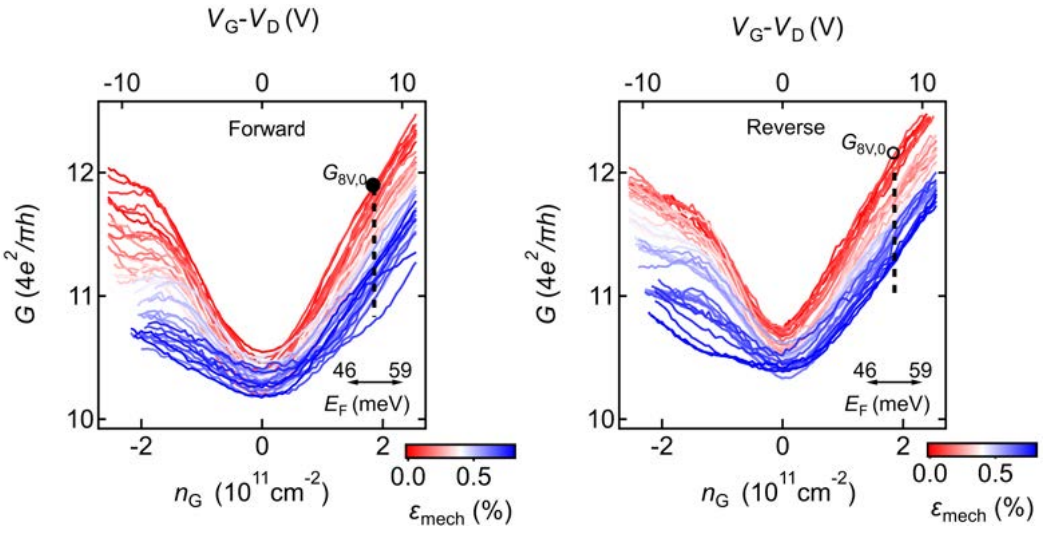

Figure 4.10: G vs $n_{\rm G}$ data for (a) forward and (b) reserse mechanical sweeps. The dashed vertical line show the location of $G_{8{\rm V},\varepsilon}$ used to analyse G vs $\varepsilon_{\rm mech}$ in detail. G_0 refers to the $\varepsilon_{\rm mech} = 0$ sweep, and the horizontal arrows show the $\tilde{E}_F$ range over which the $G_{8{\rm V},\varepsilon}$ data was averaged for analysis.

To determine $\theta_{crystal}$ and $\delta\mu_{\rm contact}$, we analyse the suppression of the experimental G vs. strain. First, we align the Dirac point of each data curve, as shown in Fig. 4.10, such that the data have the same charge density at the same $V_G - V_D$ point. Then we select a data region at large $V_G - V_D$ (so N is large), and where there is no conductance resonance (Fabry–Pérot), which will be discussed later. We average the G data around $V_G - V_D = +8$ V, covering a range $\tilde{E}_F = 46 - 59$ meV in the channel. We remark that this large $\tilde{E}_F$ exceeds significantly the estimated impurity charge density, ensuring that G is dominated by contributions from $\Delta\mu_{\rm G}$ and $\Delta\mu_\varepsilon$. Our conclusions are not depended on the exact $V_G - V_D$ position we use, as long as we avoid localized resonances and low charge density regions. We labelled this conductance $G_{8{\rm V},\varepsilon}$ and its initial value at $\varepsilon_{\rm mech} = 0$ is $G_{8{\rm V},0}$.

In Fig. 4.11, we plot $\frac{1}{G_{text8V,0} - G_{8{\rm V},\varepsilon}}$ vs. $\delta A_{y{\rm mech}}$ and fit this data using Eq. 4.10. We remark that by taking the difference $\frac{1}{G_{8{\rm V},0} - G_{8{\rm V},\varepsilon}}$, we focus on the change in resistance of the device and do not need to worry about the experimental contact resistance which is in series with $1/G$.

Now we use all parameters we obtained so far into our applied model, where $\theta_{\rm crystal} = 2.0^\circ \pm 0.4^\circ$, $n_{\rm imp} = -(1.4 \pm 0.1) \times 10^{11}$ cm^{-2}, $g_\varepsilon = 3.05 \pm 0.06$ eV, $\varepsilon_{\rm mech} = 0.8 \pm 0.2\%$, $\varepsilon_{\rm thermal} = 1.6 \pm 0.2\%$... we run a massive calculation for different chemical

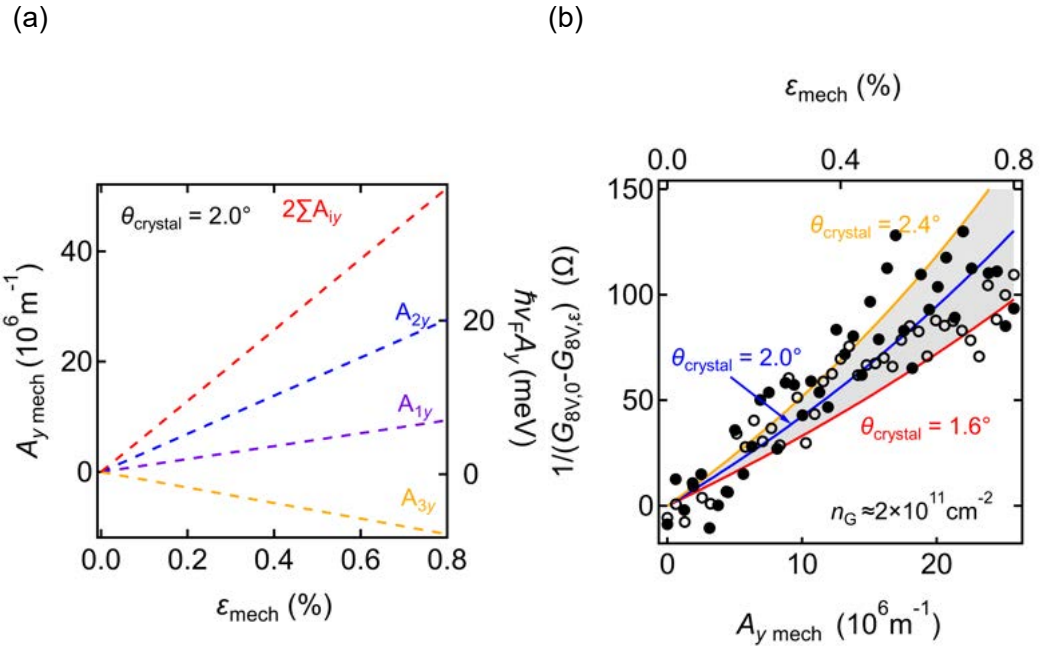

Figure 4.11: Curve fitting for crystal orientation. (a)$A_{y\text{mech}} - \varepsilon_{\text{mech}}$ data. (b)$\frac{1}{G_{8\text{V},0}-G_{8\text{V},\varepsilon}} - A_{y\text{mech}}$ data (dots) fit with Eq. 4.10 for different $\theta_{crystal}$.

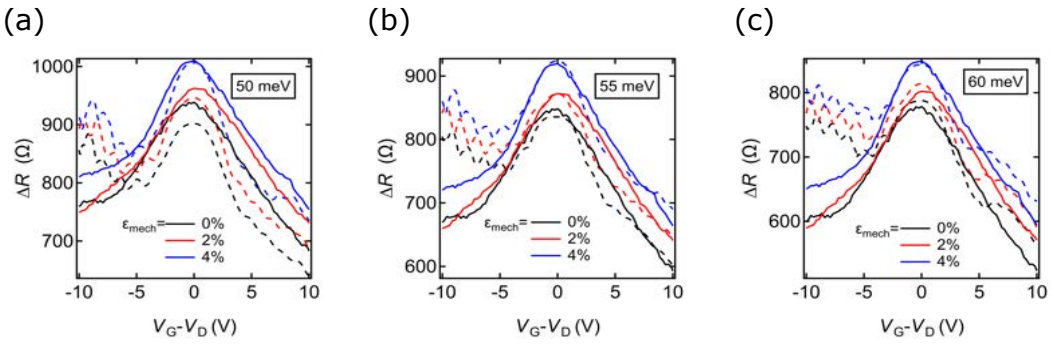

Figure 4.12: Calculated ΔR vs $V_G - V_D$ data (dash) and experimental data (solid+). (a) Calculated data with $\Delta\mu_{\text{contact}} = 50$ meV. (b)Calculated data with $\Delta\mu_{\text{contact}} = 55$ meV. (c) Calculated data with $\Delta\mu_{\text{contact}} = 60$ meV.

potential in the Lead $\Delta\mu_{\text{contact}}$. An example is given in Fig. 4.12, we calculated many value for $\Delta\mu_{\text{contact}}$ and for all curves, with emphasis on curves with lower strain (the reason will be explained later). We found $\Delta\mu_{\text{contact}} = 55$ meV best describes the reverse data and $\Delta\mu_{\text{contact}} = 50$ meV best describes the forward data.

In order to simulate our data accurately, we make an improvement to our model. Since the scalar potential changes the work function of graphene by $\Delta\mu_\varepsilon = g_\varepsilon(1-\nu)\varepsilon_{\text{total}}$, it can also cause the creation and annihilation of the allowed modes in the device. Alternatively, we could introduce a new term $\Delta\mu = \Delta\mu_{\text{contact}} + \Delta\mu_\varepsilon$, which is equivalent to a dynamic chemical potential in the lead. Therefore, when we fit for chemical potential, we aim for small strain, where $\Delta\mu_\varepsilon$ is small. We include $\Delta\mu_\varepsilon$ in our model, and plot in Fig. 4.12 (b), where the red curve is $\Delta\mu = 50\text{meV} + g_\varepsilon(1-\nu)\varepsilon_{\text{total}}$ and the blue curve is $\Delta\mu = 55\text{meV} + g_\varepsilon(1-\nu)\varepsilon_{\text{total}}$. They are in good agreement with the forward data (solid dots), and the reverse data (transparent dots). The yellow curve is a calculated curve with a constant $\Delta\mu = 45$ meV; the purple curve is a calculated curve with a constant $\Delta\mu = 65$ meV. We see the majority of the data points fall in this chemical potential range, thus it agrees with the Fermi level of the data points in Fig. 4.12 (a). It follows that the assumption for getting the fitting equation Eq. 4.10, where the energy level is roughly the same in the lead and the channel, is valid.

4.5 Combine Applied Model with Experimental Data and Beyond

In this section, we combine and compare the applied mode with experimental data. First, we calculated the last unknown parameter which is the contact resistance of the device. Then we did a full map of the applied mode to our experiment, where we found decent agreement, and we have mechanical control over the quantum interferences of our graphene transistor.

4.5.1 Determination of additional resistance

We defined:

$$R_i = R_0 + R_{\text{thermal}} + R_{\text{contact}} \tag{4.11}$$

$$R_f = R_0 + R_{\text{thermal}} + R_{\text{mech}} + R_{\text{contact}} \tag{4.12}$$

Where R_0 is the resistance of the device channel, R_{thermal} is the resistances arise by the thermal strain-induced vector potential, R_{mech} is the resistances arise by the mechanical strain-induced vector potential, R_{contact} is the additional resistances in the circuit, mostly contact resistances. R_{contact} is a constant for all the curves. Since all measurements were preformed at 0.3 K, R_{thermal} is also a constant.

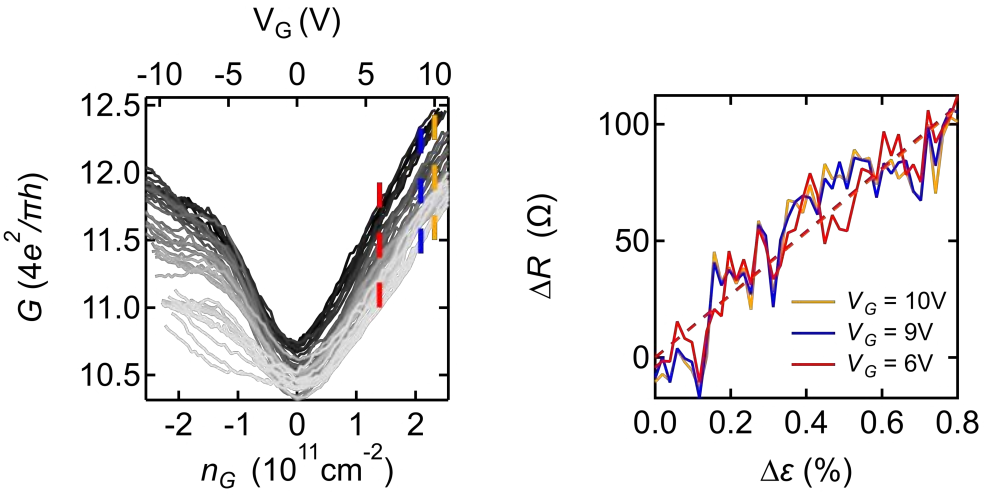

Figure 4.13: ΔR is constant. (a) we extract data at different n_G location and show (b) ΔR is the same for different n_G.

We plot ΔR vs. $\Delta\varepsilon$ in Fig.4.13 (b); this ΔR can be expressed by:

$$\Delta R = R_{\text{mech}} = \frac{h}{e^2}\left[\frac{1}{\left(\frac{4}{\pi}k_F - A_{y,f}\right)W} - \frac{1}{\left(\frac{4}{\pi}k_F - A_{y,i}\right)W}\right] \tag{4.13}$$

Where $A_{y,i}$ is the vector potential at the start of the measurement, induced by a strain $\varepsilon_i = \varepsilon_{\text{thermal}}$ and $A_{y,f}$ is the vector potential at the end of the measurement, induced by a strain $\varepsilon_f = \varepsilon_{\text{thermal}} + \varepsilon_{\text{mech}}$. We calculate $\Delta R = 105 \pm 10\Omega$, which agrees with Fig.4.13 (b).

Similarly, R_{thermal} can be expressed by:

$$R_{\text{thermal}} = \frac{h}{e^2}\left[\frac{1}{\left(\frac{4}{\pi}k_F - A_{y,i}\right)W} - \frac{1}{\left(\frac{4}{\pi}k_F - 0\right)W}\right] \tag{4.14}$$

And the additional resistance can be expressed by:

$$R_{\text{contact}} = R_i - \frac{h}{e^2}\left[\frac{1}{\left(\frac{4}{\pi}k_F - A_{y,i}\right)W} - \frac{1}{\left(\frac{4}{\pi}k_F - 0\right)W}\right] - \frac{h}{e^2}\left[\frac{1}{\left(\frac{4}{\pi}k_F - 0\right)W}\right] \tag{4.15}$$

We calculated $R_{\text{contact}} = 1100 \pm 200\Omega$.

4.5.2 Mechanical Control of Quantum Interference

In this final stage of the data analysis, we have obtained every single parameter to do the full simulation of our experiment. We plot our simulation and experimental data together in Fig. 4.14 (a), where we can see a good agreement in general.

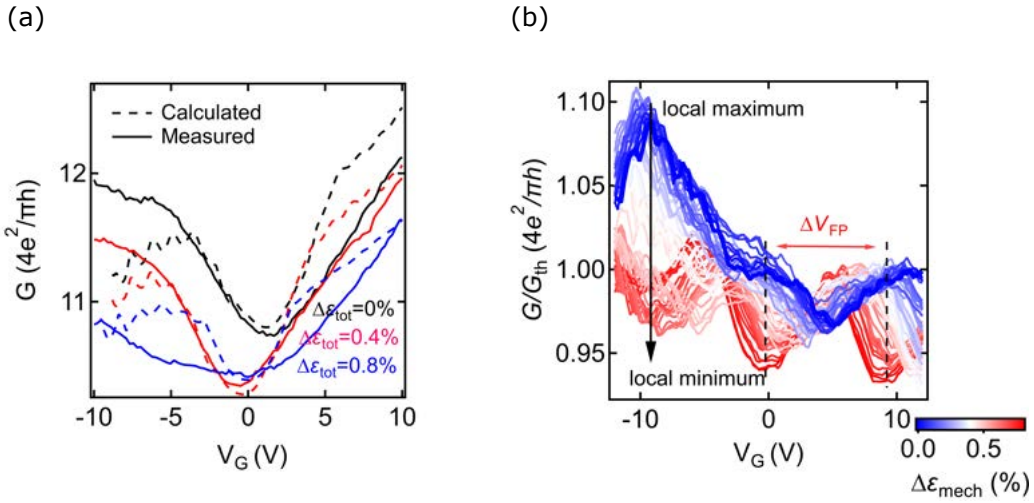

Figure 4.14: Comparison between the simulation and experimental data, and the relative conductance G/G_{th}, where we divide the experimental data with simulation data to enhance features which are not obvious in the original data set. (a) Selected curves of simulation and experimental data; the dashed curves are the simulations and the solid curves are experimental data. We found good agreement especially around the Dirac points. (b) Relative conductance versus gate voltage at different strain, where we observe the Fabry–Pérot oscillation and phase changes with increasing strain.

The Fabry–Pérot oscillation period in gate voltage, $\Delta V_{FP} = 9 \pm 1$ V, is extracted from the relative conductance $G/G_{\text{theoretical}}$ data in Fig. 4.14 (b). According to [**?**, 64],

the oscillation period should follow:

$$\Delta V_{FP} = \frac{e}{c_G} \frac{2a}{1 + aL\sqrt{\frac{e}{\pi c_G V_{FP}}}} \tag{4.16}$$

Where $L = 90$ nm is the device channel length, C_G is the gate capacitance per unit area. The barrier parameter is calculated to be $a = 0.009756$ nm^{-2}. And a can also be expressed with:

$$a = \frac{\sqrt{\pi} V_0}{\zeta_F d} \tag{4.17}$$

Where $\zeta_F = \sqrt{\pi}\hbar V_F / e$ is the Fermi electric flux and eV_0 is the difference of the Fermi energies of the suspended graphene channel and the graphene under the contact. In our case $eV_0 = \Delta\mu_{\text{contact}} - \Delta\mu_G$, thus:

$$d = \frac{\Delta\mu_{\text{contact}} - \Delta\mu_G}{\hbar V_F a} \tag{4.18}$$

We calculate $d = 8 \pm 1$ nm for $V_G = 0$ V. In our simulation, we assume a sharp potential step (straight barrier) for a 90 nm cavity, shown as blue lines in Fig. 4.15. However, in reality, our device has a triangular barrier, shown as yellow lines in Fig. 4.15, where the transition of energy level occur in range with length d. This is the primary cause for difference between our simulation and experimental data. Moreover, it is obvious that d is smaller in the positive gate voltage side and d is larger in the negative gate voltage side when $\Delta\mu_G$ become negative. This also explains why the simulation and the experiment data agree more on one side than the other.

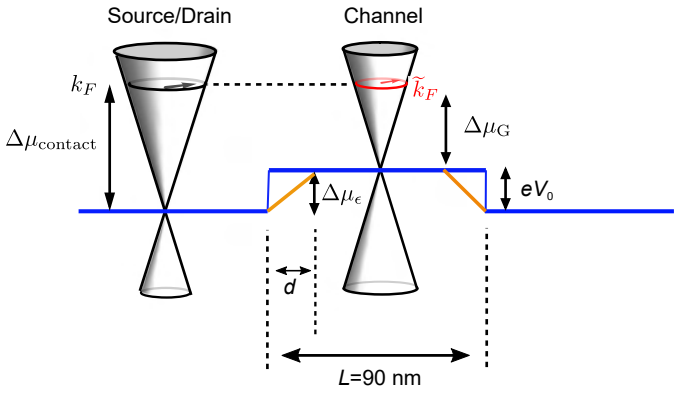

Figure 4.15: Schematic view of the energy levels in the Device for a special case where the energy in the source is the same as the energy in the channel.

We also observe phase changes with increasing strain in Fig. 4.14 (b). The curves change from local maximum to local minimum at $V_G = \pm 10$ V and $V_G = 0$ V. It is possible that this phase shift is cause by an Aharonov–Bohm-like effect. Given our vector potential describe in Eq. 2.5, Our $\boldsymbol{A}_{y,i}$ has zero curl. More experiments needed to confirm this discovery.

Chapter 5

Conclusions and Prospects

We have demonstrated that by combining an applied theory for transport in graphene quantum strain transistors reported in Chapter 2 and our experimental data in nearly identical devices reported in Chapter 4, we were able to understand the dominant effects of uniaxial strain in graphene FET's. By straining graphene mechanically with two gold cantilever mechanical clamps and measuring the channel's conductance, we investigated the predicted strain-induced scalar and vector potentials. Comparison of experimental data and theory showed quantitative agreements, even with zero free parameter in the model. We also demonstrated mechanical control over quantum interferences in a graphene transistor. In this conclusion, we begin with a brief review of our main results as described in Chapters 2, 3 and 4, as well as their implications for the design of the next round of graphene quantum strain transistors. Finally, we end with a discussion of the next steps for this project to improve both experimental and theoretical results, and discuss what is possible in future experiments.

5.1 Main Results: Rigorous Data Analysis to Connect GQST Theory and Experiment

We presented in Chap 2 an applied GQST theoretical framework, including previously neglected device parameters changing the expected transport [1] dramatically, to understand the physics explored throughout this thesis. We began with a description of how uniaxial strain modifies graphene's lattices and its band structure. We observed that the strain-induced scalar potential changes the graphene's work function and

shifts the channel's Fermi energy. We also clearly demonstrated that strain-induced vector potential arise from both lattice distortion and shifts in hopping energies. We then calculated conductance in graphene and SWCNT quantum strain transistor. We show the conductance decreases and the conductance minimum shifts toward the negative gate voltage with increasing strain. We use these concepts as a basis to quantitatively understand and interpret our data in Chapter 4.

We presented in Chap 3 our fabrication methods and devices, our custom instrument capable of *in situ* strain control, low temperatures transport measurements with sub pico-Ampere precision. Our fabrication process produces high quality graphene devices with low structural disorder. For graphene break-junction, the channel length can down to ≈10 nm, while for graphene gap-junction, the channel length can down to ≈100 nm. We also fabricate devices up to several microns to allow optical and electromechanical resonances measurements [57, 59].

In Chapter 4, we presented the main results of this thesis, where we carefully presented original data analysis of a detailed experiment on a GQST device. Exploring the transport data and developing data analysis methods based on our theoretical understanding, we showed that we applied a mechanical strain up to 0.8 % in a channel whose $\theta_{crystal} = 2^\circ$, $n_{imp} \approx -1.4 \times 10^{11}$ cm^{-2}, $R_{\text{contact}} = 1100\Omega$, and $\delta\mu_\varepsilon$ was mechanically tunable from 45 meV to 65 meV. We found clear evidence for quantitatively accurate strain-induced scalar and vector potentials. By analyzing the shift of the conductance minimum in $G - V_{\text{G}}$ data sets and the suppression of the conductance, we observed strain-induced vector potentials up to 24 $\times 10^6$ m^{-1}. By comparing theoretical predictions with the experiment, we argue that their modest discrepancies in same parameter ranges arise from different Fabry–Pérot cavity lengths. In our model, we used a fixed cavity length of 90 nm. In our experiment, we found that the cavity length is dependent on the Fermi level in the channel and electrostatic barrier shape. We demonstrated unprecedented mechanical control of transmissions and quantum interferences in our graphene transistor.

5.2 Prospects for Strain-Engineered QNEMS

In the short term, we will continue our ongoing project to use uniaxial strain in suspended graphene aiming to completely turn on/off its charge conductivity. We

predicted high on/off ratio GQSTs in Chapter 2 and Ref. [1], but have not yet realized them. However, given by the experiment reported in Chapter 4, which validates our applied model, we are confident to achieve this goal with optimized device fabrication. We can improve our fabrication by combining polarized Raman characterization [42] and dry stamping techniques [65] to identify the crystal orientation of the graphene flakes ahead of contact deposition. The crystal orientation plays significant role in maximizing the strain effects. Moreover, our new generation of transistor will have a much higher gating efficiency due to a SiO_2 layer maximizing C_G. We also plan expand our experiments to apply tunable strains to quantum SWCNT transistors. We aim to mechanically tailor the band gaps, QD charging energies and QD electron hole asymmetry in SWCNTs. We are very likely to achieve single electron strain transistors through such experiment.

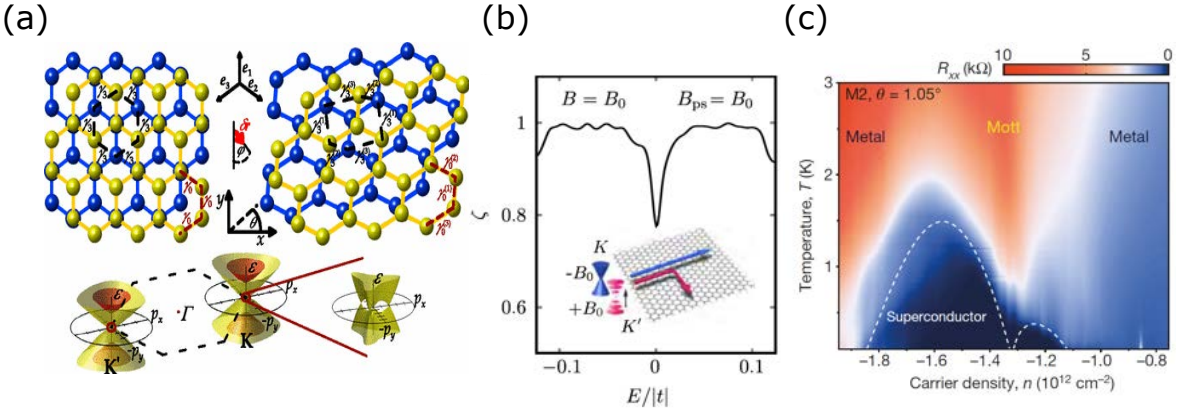

Figure 5.1: Ideas for future experiments. (a) Top: Unperturbed (left) and strained (right) bilayer graphene lattice. The top and bottom graphene layers are shown in yellow and blue, respectively. Bottom: Electronic band structure of strained bilayer graphene in the vicinity of the Brillouin zone corners K and K'. Figure adapted from Ref. [66].(b) Valley polarization (ζ) as a function of Fermi energy in graphene with equal magnetic (B) and pseudomagnetic (B_{ps}) fields. Inset: The magnetic and pseudomagnetic fields add for one valley and cancel out for the other, creating a valley filter. Figure adapted from Ref. [25]. (c) Color plot of $T - n - R$ showing unconventional superconductivity in twisted bilayer graphene. Figure adapted from Ref. [67].

In the longer term, we will experimentally explore uniaxial strain effects on transport in bilayer graphene. Recent study predicted that strain trigger a Lifshitz transition in bilayer graphene [68]. It is a transition of the Dirac cone topology where each K valley acquires 3 cones near the charge neutrality point [69], as shown in

Fig. 5.1(a). An uniaxial strain of 1% is expected to induce observable strain effects [66], which is within the capability of our measurement platform.

Unconventional superconductivity was found in a twisted bilayer graphene where two monolayer graphene are stamped onto one another with a $\theta \approx 1.05^\circ$ rotation. The reported $R-T-n$ phase diagram is shown in Fig. 5.1(c). We could apply mechanical stain to accurately tune the rotation angle θ *in situ* and control the superconducting phase transitions. It would offer a unique opportunity to engineer and explore the graphene superconducting phase diagram.

We can also modify our sample holder and nanofabrication to apply triaxial strains. This will result in a large and tunable pseudomagnetic fields, leading to quantum Hall effects and Landau level physics at room temperature [23, 70]. By combining real and pseudomagnetic fields, it is theoretically possible to create a valley filter in graphene, where only electrons of a given valley could pass through the device [25]. This theoretical prospect is shown in Fig. 5.1 (b), adapted from Ref. [25], where the valley polarization (ζ) is plotted as a function of carrier energy for equal magnitudes of magnetic ($B = B_0$) and pseudomagnetic ($B_{\text{ps}} = B_0$) fields. Polarization is nearly unity for a wide range of energies, indicating a robust valley filtering effect. The inset shows the mechanism of this valley filter. Since the pseudomagnetic field has opposite sign in the two valleys, the sum of the magnetic and pseudomagnetic fields is $2B_0$ for one valley and 0 for the other. This introduces Landau gaps in the spectrum of one valley and not the other, allowing pure valley filtering.

In conclusion, we have taken a first step in exploring the quantum "mechanics" of 2D transport, and this field remains widely unexplored.

Bibliography

[1] A. McRae, G. Wei, and A. Champagne, *Graphene Quantum Strain Transistors*, Phys. Rev. Applied **11**, 054019 (2019).

[2] J. H. Warner, F. Schäffel, A. Bachmatiuk, and M. H. Rümmeli, Chapter 6 - applications of graphene, in *Graphene*, edited by J. H. Warner, F. Schäffel, A. Bachmatiuk, and M. H. Rümmeli, pages 333 – 437, Elsevier, (2013).

[3] Y. Sun, M. Sun, and D. Xie, 5 - graphene electronic devices, in *Graphene*, edited by H. Zhu, Z. Xu, D. Xie, and Y. Fang, pages 103 – 155, Academic Press, (2018).

[4] A. Tan, R. Jeyaraj, and S. De Lacey, Chapter 7 - nanotechnology in neurosurgical oncology, in *Nanotechnology in Cancer*, edited by A. B. Mathur, Micro and Nano Technologies, pages 139 – 170, William Andrew Publishing, (2017).

[5] Z. Moktadir, 14 - graphene nanoelectromechanics (nems), in *Graphene*, edited by V. Skákalová and A. B. Kaiser, pages 341 – 362, Woodhead Publishing, (2014).

[6] A. A. Bukharaev, A. K. Zvezdin, A. P. Pyatakov, and Y. K. Fetisov, *Straintronics: a new trend in micro- and nanoelectronics and materials science*, Physics-Uspekhi **61**, 1175 (2018).

[7] Z. Lin et al., *Research Update: Recent progress on 2D materials beyond graphene: From ripples, defects, intercalation, and valley dynamics to straintronics and power dissipation*, APL Materials **6**, 080701 (2018).

[8] W. Yan, *Conductance modulated by the strain in normal metal–graphene junctions*, Results in Physics , 103723 (2020).

[9] N. D'Souza et al., *Energy-efficient switching of nanomagnets for computing: straintronics and other methodologies*, Nanotechnology **29**, 442001 (2018).

[10] M. M. Fogler, F. Guinea, and M. I. Katsnelson, *Pseudomagnetic fields and ballistic transport in a suspended graphene sheet*, Phys. Rev. Lett. **101**, 226804 (2008).

[11] L. Li, Y. Wang, Z. Wang, Y. Liu, and B. Wang, *Topological Insulator GMR Straintronics for Low-Power Strain Sensors*, ACS Applied Materials & Interfaces **10**, 28789 (2018).

[12] E. O. Savostin and N. A. Pertsev, *Superconducting straintronics via the proximity effect in superconductor–ferromagnet nanostructures*, Nanoscale **12**, 648 (2020).

[13] D. Akinwande et al., *A review on mechanics and mechanical properties of 2D materials-Graphene and beyond*, Extreme Mech. Lett.s **13**, 42 (2017).

[14] A. H. Castro Neto, F. Guinea, N. M. R. Peres, K. S. Novoselov, and A. K. Geim, *The electronic properties of graphene*, Rev. Mod. Phys. **81**, 109 (2009).

[15] G. G. Naumis, S. Barraza-Lopez, M. Oliva-Leyva, and H. Terrones, *Electronic and optical properties of strained graphene and other strained 2D materials: a review*, Rep. Prog. Phys. **80**, 096501 (2017).

[16] M.-F. Yu et al., *Strength and breaking mechanism of multiwalled carbon nanotubes under tensile load*, Science **287**, 637 (2000).

[17] A. McRae, *Graphene Quantum Strain Transistors and Two-in-One Carbon Nanotube Quantum Transistors*, PhD thesis, Concordia University, (2018).

[18] L. Banszerus et al., *Ballistic transport exceeding 28 μm in CVD grown graphene*, Nano Lett. **16**, 1387 (2016).

[19] S. Chen et al., *Electron optics with p-n junctions in ballistic graphene*, Science **353**, 1522 (2016).

[20] A. Javey et al., *High performance n-type carbon nanotube field-effect transistors with chemically doped contacts*, Nano Lett. **5**, 345 (2005).

[21] M. M. Shulaker et al., *Carbon nanotube computer*, Nature **501**, 526 (2013).

[22] Z.-Z. Cao, Y.-F. Cheng, and G.-Q. Li, *Strain-controlled electron switch in graphene*, App. Phys. Lett. **101**, 253507 (2012).

[23] F. Guinea, M. I. Katsnelson, and A. K. Geim, *Energy gaps and a zero-field quantum Hall effect in graphene by strain engineering*, Nat. Phys. **6**, 30 (2010).

[24] C.-C. Hsu, M. L. Teague, J.-Q. Wang, and N.-C. Yeh, *Nanoscale strain engineering of giant pseudo-magnetic fields, valley polarization, and topological channels in graphene*, Science Advances **6** (2020).

[25] M. Settnes, J. H. Garcia, and S. Roche, *Valley-polarized quantum transport generated by gauge fields in graphene*, 2D Mat. **4**, 031006 (2017).

[26] Y. Jiang et al., *Visualizing strain-induced pseudomagnetic fields in graphene through an hBN magnifying glass*, Nano Lett. **17**, 2839 (2017).

[27] A. Georgi et al., *Tuning the pseudospin polarization of graphene by a pseudomagnetic field*, Nano Lett. **17**, 2240 (2017).

[28] K. S. Kim et al., *Large-scale pattern growth of graphene films for stretchable transparent electrodes*, Nature **457**, 706 (2009).

[29] L. Wang et al., *In Situ Strain Tuning in hBN-Encapsulated Graphene Electronic Devices*, Nano Letters **19**, 4097 (2019).

[30] Y. Zhang et al., *Strain modulation of graphene by nanoscale substrate curvatures: a molecular view*, Nano Lett **18**, 2098 (2018).

[31] M. Guo, Y. Qian, H. Qi, K. Bi, and Y. Chen, *Experimental measurements on the thermal conductivity of strained monolayer graphene*, Carbon **157**, 185 (2020).

[32] N. Levy et al., *Strain-induced pseudo-magnetic fields greater than 300 tesla in graphene nanobubbles*, Science **329**, 544 (2010).

[33] C. Lee, X. Wei, J. W. Kysar, and J. Hone, *Measurement of the elastic properties and intrinsic strength of monolayer graphene*, Science **321**, 385 (2008).

[34] T. M. G. Mohiuddin et al., *Uniaxial strain in graphene by Raman spectroscopy: G peak splitting, Grüneisen parameters, and sample orientation*, Phys. Rev. B **79**, 205433 (2009).

[35] M. Goldsche et al., *Tailoring mechanically tunable strain fields in graphene*, Nano Lett **18**, 1707 (2018).

[36] C. Chen et al., *Performance of monolayer graphene nanomechanical resonators with electrical readout*, Nat. Nanotechnol. **4**, 861 (2009).

[37] D. Metten, G. Froehlicher, and S. Berciaud, *Monitoring electrostatically-induced deflection, strain and doping in suspended graphene using Raman spectroscopy*, 2D Mat. **4**, 014004 (2016).

[38] F. M. D. Pellegrino, G. G. N. Angilella, and R. Pucci, *Transport properties of graphene across strain-induced nonuniform velocity profiles*, Phys. Rev. B **84**, 195404 (2011).

[39] Y. Q. Wu et al., *Quantum behavior of graphene transistors near the scaling limit*, Nano Lett. **12**, 1417 (2012).

[40] A. C. McRae, V. Tayari, J. M. Porter, and A. R. Champagne, *Giant electron-hole transport asymmetry in ultra-short quantum transistors*, Nat. Commun. **8**, 15491 (2017).

[41] J. Tworzydlo, B. Trauzettel, M. Titov, A. Rycerz, and C. W. Beenakker, *Sub-Poissonian shot noise in graphene*, Phys. Rev. Lett. **96**, 246802 (2006).

[42] M. Huang et al., *Phonon softening and crystallographic orientation of strained graphene studied by Raman spectroscopy*, Proc. Natl. Acad. Sci. U.S.A. **106**, 7304 (2009).

[43] E. Y. Andrei, G. Li, and X. Du, *Electronic properties of graphene: a perspective from scanning tunneling microscopy and magnetotransport*, Rep. Prog. Phys. **75**, 056501 (2012).

[44] A. R. Champagne, A. N. Pasupathy, and D. C. Ralph, *Mechanically adjustable and electrically gated single-molecule transistors*, Nano Lett. **5**, 305 (2005).

[45] F. C. Nix and D. MacNair, *The thermal expansion of pure metals: copper, gold, aluminum, nickel, and iron*, Phys. Rev. **60**, 597 (1941).

[46] V. Singh et al., *Probing thermal expansion of graphene and modal dispersion at low-temperature using graphene nanoelectromechanical systems resonators*, Nanotechnology **21**, 165204 (2010).

[47] D. Yoon, Y. W. Son, and H. Cheong, *Negative thermal expansion coefficient of graphene measured by Raman spectroscopy*, Nano Lett. **11**, 3227 (2011).

[48] A. Kretinin et al., *Quantum capacitance measurements of electron-hole asymmetry and next-nearest-neighbor hopping in graphene*, Phys. Rev. B **88**, 165427 (2013).

[49] M. A. H. Vozmediano, M. I. Katsnelson, and F. Guinea, *Gauge fields in graphene*, Phys. Rep. **496**, 109 (2010).

[50] S.-M. Choi, S.-H. Jhi, and Y.-W. Son, *Effects of strain on electronic properties of graphene*, Phys. Rev. B **81** (2010).

[51] D. C. Elias et al., *Dirac cones reshaped by interaction effects in suspended graphene*, Nature Physics **7**, 701 (2011).

[52] A. L. Kitt, V. M. Pereira, A. K. Swan, and B. B. Goldberg, *Erratum: Lattice-corrected strain-induced vector potentials in graphene [Phys. Rev. B85, 115432 (2012)]*, Phys. Rev. B **87**, 159909 (2013).

[53] D. Fathi and A. Kumar, *A Review of Electronic Band Structure of Graphene and Carbon Nanotubes Using Tight Binding*, Journal of Nanotechnology **2011**, 1687 (2011).

[54] L. Yang, M. P. Anantram, J. Han, and J. P. Lu, *Band-gap change of carbon nanotubes: Effect of small uniaxial and torsional strain*, Phys. Rev. B **60**, 13874 (1999).

[55] L. Yang and J. Han, *Electronic Structure of Deformed Carbon Nanotubes*, Phys. Rev. Lett. **85**, 154 (2000).

[56] P. Blake et al., *Making graphene visible*, Applied Physics Letters **91**, 063124 (2007).

[57] M. Stroms, *Electromechanical Resonances in Suspended Bilayer Graphene*, PhD thesis, Concordia University, (2019).

[58] A. C. Ferrari and D. M. Basko, *Raman spectroscopy as a versatile tool for studying the properties of graphene*, Nat. Nanotechnol. **8**, 235 (2013).

[59] G. Melin, *Spatial Dependence of Photocurrent and Photogeneration Mechanisms in Graphene Field Effect Transistors*, PhD thesis, Concordia University, (2019).

[60] G. K. Goswami and K. K. Nanda, *Electrical breakdown of carbon nanotube devices and the predictability of breakdown position*, AIP Adv. **2**, 022129 (2012).

[61] G. Lene et al., *Graphene transport properties upon exposure to PMMA processing and heat treatments*, 2D Mat. **1**, 035005 (2014).

[62] D. Bahamon and V. M. Pereira, *Conductance across strain junctions in graphene nanoribbons*, Phys. Rev. B **88**, 195416 (2013).

[63] F. M. D. Pellegrino, G. G. N. Angilella, and R. Pucci, *Transport properties of graphene across strain-induced nonuniform velocity profiles*, Phys. Rev. B **84**, 195404 (2011).

[64] Y. Liu et al., *Dry transfer method for suspended graphene on lift-off-resist: simple ballistic devices with Fabry–Pérot interference*, Nanotechnology **30**, 25LT01 (2019).

[65] A. Castellanos-Gomez et al., *Deterministic transfer of two-dimensional materials by all-dry viscoelastic stamping*, 2D Mat. **1**, 011002 (2014).

[66] M. Mucha-Kruczyński, I. L. Aleiner, and V. I. Fal'ko, *Strained bilayer graphene: Band structure topology and Landau level spectrum*, Phys. Rev. B **84**, 041404 (2011).

[67] Y. Cao et al., *Unconventional superconductivity in magic-angle graphene superlattices*, Nature **556**, 43 (2018).

[68] A. Varlet et al., *Tunable Fermi surface topology and Lifshitz transition in bilayer graphene*, Synthetic Metals **210**, 19 (2015).

[69] E. McCann and V. I. Fal'ko, *Landau-Level Degeneracy and Quantum Hall Effect in a Graphite Bilayer*, Phys. Rev. Lett. **96**, 086805 (2006).

[70] M. Settnes, S. R. Power, and A.-P. Jauho, *Pseudomagnetic fields and triaxial strain in graphene*, Phys. Rev. B **93**, 035456 (2016).